Bachelor's thesis

Ice formation in supercooled stratiform clouds over the Swiss Plateau

Anja Marie Hardt

Freiberg, 15.07.2024

TU Bergakademie Freiberg

Supervisors:	Dr. Frank Zimmermann, Dr. Patric Seifert
Examiners:	Dr. Frank Zimmermann, Dr. Patric Seifert
Course:	Bachelor of Geoecology - Environmental Sciences

Declaration of Authorship

I declare, that I have authored this work on my own under the guidance of my supervisors. I have not used any other tools than the declared. Parts of the work, which are taken from other works, if literally or in sense, I have cited correctly under specification of the source in each single case. This declaration also applies on images and figures. I declare, that this work satisfies the principles of academic integrity. I declare, that this work has not been presented to any other examination board, nor it will be.

Freiberg, July 17, 2024

Anja Marie Hardt

Abstract

Aerosol-cloud interactions play an important role in local weather as well as in the global climate. Ice nucleating particles (INP), a subset of all aerosols particles are needed for the formation of ice crystals in the temperature range of ca. –38 °C to 0 °C. This property assigns these particles an important role in the formation of precipitation, as ice attracts water vapour more efficiently than water droplets. Without INP, clouds in the given temperature range would consist of supercooled water droplets only. As the number of INP in the atmosphere is low, perturbations in their properties can have a significant impact on heterogeneous ice nucleation in clouds. This is directly impacting the abundance of ice crystals in liquid water clouds. The formation of ice crystals through the activation of INP leads to a depletion of INP in the air mass if the ice crystals fall as precipitation. This Bachelor's thesis is investigating both effects through a constellation of two measurement sites occasionally situated along one air mass trajectory. This allowed the investigation of depletion of INP in the air mass during transport. The measurement periods were characterized by the presence of a supercooled liquid cloud layer (Temperature between 0 °C and –10 °C) and a liquid cloud layer with cloud top temperature around 0 °C over the Swiss Plateau. The concentration of ice nucleating particles in air masses during the presence of this cloud was analysed in this work. For the determination of spatial differences, the same analysis was performed for air masses over south Germany, the origin of the air masses during the formation of the stratiform cloud. The low stratiform cloud is occurring as a local weather phenomenon in winter times under the condition of north-eastern winds, the so-called Bise winds. This thesis is aiming to contribute to the understanding of the role of ice nucleating particles in the persistence of the low stratiform cloud over the Swiss Plateau.

In this work data from Eriswil in the Swiss Plateau is compared with data of Hohenpeißenberg in the south of Germany, situated northeast of Eriswil. Filter samples and remote-sensing data was taken by the Leibniz Institute for Tropospheric Research (TROPOS) and the German Meteorological Service (DWD) during two research time periods, 06.01.2024–12.01.2024 and 27.02.2024–01.03.2024. The remote-sensing data was used for the analysis of physical atmospheric properties during the research period of each research site. Air mass trajectories for Hohenpeißenberg and Eriswil were calculated and analysed. The filter samples were analysed in the Ice Laboratory at TROPOS to determine the concentration and the heat lability of ice nucleating particles in the air at the research site. The results show a dependence of heat labile INP from the origin of air masses and the ambient temperatures during sampling. A spatial contrast between Hohenpeißenberg and Eriswil in the concentration of INP was found in samples with a high heat labile fraction in Hohenpeißenberg and low ambient temperatures during sampling. No spatial contrast was found in samples with a low heat labile fraction in Hohenpeißenberg and high ambient temperatures during sampling.

List of Figures

List of Abbreviations

Abbrevation	Explanation
DFA	Droplet Freezing Array
DWD	German Meteoroglical Service (Deutscher Wetterdienst)
INDA	Ice Nucleation Droplet Array
INP	Ice Nucleating Particle
IWV	Integrated Water Vapor
LACROS	Leipzig Aerosol and Cloud Observations System
LINA	Leipzig Ice Nucleation Array
LWP	Liquid Water Path
PBL	Planetary Boundary Layer
PRF	Pulse Repetition Frequency
TROPOS	Leibniz-Institute for Tropospheric Research
UV	Ultraviolet
VIS	Visible Radiation
VISSS	Video in Situ Snowfall Sensor

Contents

1 Introduction

Precipitation and clouds play a major role in the hydrological cycle, the local weather as well as the global climate. With varying properties, clouds can impact the climate through a warming or cooling influence due to a varying albedo. Fully understanding the properties and micro-processes in clouds is therefore very important for understanding the climate system. The research of Zhang (2010) showed that the prediction of cloud appearance by model outputs, compared to cloud observations via satellite is inaccurate. Further research is needed for more detailed information about the formation and dissolving processes of clouds.

Even though the mass fraction of ice in the atmosphere is low, it influences many atmospheric processes like precipitation, cloud electrification, and radiative transfer (Cantrell & Heymsfield, 2005). Precipitation in the middle and high latitudes generally forms through the ice phase (Schönwiese, 2013). More than half of the clouds at temperatures of –15 °C to –20 °C contain ice (Hoose & Möhler, 2012). Most clouds in the lower to middle troposphere are therefore mixed-phase clouds, consisting of supercooled liquid water droplets and ice crystals. Ice formation in clouds is of crucial importance for the global climate. The processes of ice nucleation, needed for ice formation in clouds, are still poorly understood (Holden et al., 2021).

1.1 Research Context

In the Swiss Plateau, permanent and resistant low stratiform clouds and high fog clouds are a typical appearance in spring and wintertime, due to the so-called Bise winds. The Bise is a regional north-, northeast- or east- wind in the Alpine mountains area, occurring due to the presence of a high-pressure area north of the Alps and a low-pressure area in Eastern Europe. This enforces the north-south or northeast-southwest surface pressure gradient. The Bise is a result of multiple factors. A west to east moving cyclone as well as an anticyclone north of the Alps is required to be present. The frontal and postfrontal weather conditions of the cyclone are influenced by the orography of the Jura and the Alpine mountains. A combination of these factors is responsible for the Bise situation. The Bise leads to cold winds with high wind speeds and anticyclonic weather conditions (Wanner & Furger, 1990).

The Bise wind situation is often accompanied by formation of a stable stratiform cloud deck over the Swiss Plateau. As precipitation in these latitudes is mainly formed through the ice phase, ice formation is crucial for any dissolution process of these clouds to take place. Observations show, that only every tenth stratiform cloud situation in the Swiss Plateau forms precipitation (Granwehr, 2022). The low-cloud cover is formed at temperatures of down to –10 °C, which should allow ice formation at low heights above ground. The observed ice content in the supercooled low clouds over the Swiss Plateau is way lower than expected. The lack of ice formation leads to a lack of precipitation from these clouds, which complicates regional weather forecasts. The persistence of these clouds is hardly predictable. Reasons for the low ice content in the low supercooled clouds remain unclear. Further research is needed to understand the lack in ice formation in low supercooled clouds over the Swiss Plateau, to improve local weather models and precipitation forecasts.

Hoose and Möhler (2012) among others showed, that biological ice nucleating particles (INP) are effective in ice nucleation above –10 °C. Biological INP are limited in winter times due to vegetation being inactive. This leads to the hypothesis, that the lack of ice formation in the supercooled low clouds over the Swiss Plateau is due to a lack of effective INP in the temperature range present in the low clouds. For investigating this hypothesis, the air masses of two research sites at upwind and downwind location of the Swiss Plateau were sampled, and a freezing analysis was performed for each sample.

During the CLOUDLAB-Campaign the ice nucleation in the clouds over Eriswil in the Swiss Plateau was investigated via in situ measurements and remote-sensing observations. INP were injected into the clouds to enforce ice nucleation (cloud seeding, see Sect. 2.5). In situ and ground-based remote-sensing instrumentation was used for investigating microphysical changes due to the seeding activities (Henneberger et al., 2023).

1.2 Research Goal and Hypothesis

The goal of this thesis is the investigation of a potential spatial contrast in the ice formation in supercooled stratiform clouds over the Alpine highlands of southern Germany and Switzerland. This research is aiming to contribute to the understanding of the regional weather phenomenon of the permanent stratiform high fog Bise clouds of the Swiss Plateau. For reaching this goal a freezing analysis was performed on air samples taken in the Alpine highlands of southern Germany (Hohenpeißenberg) and the Swiss Plateau

(Eriswil). The freezing analysis is supported by remote-sensing data, provided by instrumentation related to the PolarCAP-Campaign and the third edition of the CLOUDLAB-Campaign. In the context of the CLOUDLAB-Campaign, ice nucleation was enforced using silver iodide (AgI). This thesis is also evaluating the effects of these injections on the freezing behavior of the taken air samples.

This thesis is aiming to support or refute the following hypotheses:

- The air masses passing south Germany in a north-east-wind situation, are losing INP on their way to the Swiss Plateau.
- The performed seeding activity using silver iodide (AgI) by the CLOUDLAB-Campaign does not affect the freezing behavior of the taken air samples.

Further explanations about ice formation processes in clouds, including heterogeneous and homogeneous ice nucleation are given in the following chapter (Chapter 2: Fundamentals). In this chapter also the formation of precipitation through the ice phase in mixed-phase clouds as well as the induced ice formation in clouds (cloud seeding) is explained. Further information about the practical part of this thesis is given in chapter 3: Instruments and Methods. The chapter is beginning with the sampling process and the used instrumentation, including a description of underlying processes for radar, lidar, and the Video in Situ Snowfall Sensor (VISSS). This part is followed by basic information concerning air mass trajectories and the used measuring devices for the off-line immersion freezing analysis. After the explanation of the freezing experiments, the calculation of INP is explained. The results of the freezing experiments are presented in chapter 4: Results; along with selected remote-sensing data and calculated trajectories for the determination of air mass movements. The results are discussed and interpreted within chapter 5: Discussion. The discussion of results is followed by conclusions including a proposal for further research topics in chapter 6: Conclusions.

2 Fundamentals

For the investigation of the ice formation in low stratiform clouds over the Swiss Plateau, it is important to understand the fundamental processes of ice formation in the troposphere. The primary formation of ice in the atmosphere can take place via two processes, homogeneous and heterogeneous ice nucleation. Both are explained in more detail below, in section 2.1 and 2.2 respectively. After the primary formation of an ice crystal in a cloud, its fate is influenced by many parameters and processes (see section 2.3 and 2.4). Finally, section 2.5 gives an overview of natural and anthropogenic seeding processes, describing the enforced ice formation in clouds.

2.1 Homogeneous Ice Nucleation

Homogeneous ice nucleation describes the process of ice nucleation as a spontaneous event in a pure liquid (Cantrell & Heymsfield, 2005). As the phase change from the liquid to the solid phase is an energy consuming process (due to the free energy barrier), the existence of a primary ice crystal is energetically unfavourable (Fletcher, 2009). Therefore, ice in the atmosphere is a consequence of a nucleation process (Cantrell & Heymsfield, 2005). Homogeneous nucleation of ice appears mainly in the upper troposphere in updrafts of high cumulus clouds, since it is limited to temperatures below ca. –38 °C (Hoose & Möhler, 2012). At temperatures above ca. –38 °C ice formation is dominated by the heterogeneous ice nucleation process.

2.2 Heterogeneous Ice Nucleation

Heterogeneous ice nucleation describes the process of ice nucleation at temperatures at which no homogeneous ice nucleation occurs. The heterogeneous ice nucleation is catalysed by a foreign substance, called ice nucleating particle (INP, Hoose and Möhler, 2012). INPs act as a substrate for ice nucleation, which lowers the energy barrier between the solid and liquid or vapour phase. This enables ice formation in the atmosphere at temperatures above the homogeneous freezing temperatures.

Historically, four kinds of heterogeneous freezing processes were distinguished: immersion freezing, contact freezing, condensation nucleation, and deposition nucleation (S. Hartmann et al., 2011). Contact freezing describes the ice nucleation at a triple interface consisting of water, air, and a particle. This triple interface forms when a foreign particle hits a supercooled droplet (Vali et al., 2015). Condensation nucleation describes the ice nucleation through the cloud condensation nuclei, instantaneously after droplet formation (Seifert, 2011).

Recently, only two freezing modes are distinguished: immersion freezing and deposition freezing (Holden et al., 2021). In immersion freezing ice nucleation takes place within the droplet. The nucleation is catalysed by an INP dispersed in the supercooled droplet. This particle can be the initial cloud condensation particle or an immersed particle (S. Hartmann et al., 2011). In deposition freezing, water vapour deposits at the surface of an INP. The vapour freezes immediately, without a liquid phase. Deposition freezing requires low values of supersaturation and takes place at low temperatures of ca. –38 °C (Hoose & Möhler, 2012).

2.3 Ice Formation in Mixed-phase Clouds

Mixed-phase clouds are characterized by the coexistence of supercooled liquid droplets and ice crystals. The existance of mixed-phase clouds is limited to temperatures above ca. -38 °C, where homogeneous ice nucleation does not occur. The existance of ice crystals in mixed-phase clouds is enabled via the heterogeneous ice nucleation process with the aid of an INP. If ice is formed at an INP surface, the INP is devoted to be activated. The supercooled liquid drops of a cloud and/or water vapour accumulate at the INP, inducing the growth of the ice crystal. The crystal grows until the gravitational force exceeds forces of uplifting air motions. The crystal falls as precipitation. Depending on the temperature gradient on the way down and the height of the melting point, the crystal melts and falls as raindrop (Schönwiese, 2013).

The fraction of aerosol particles able to act as INP is small. At a temperature of -20 °C the fraction of aerosols able to act as INP is on average $1 : 10^6$. Different types of aerosol particles can act as INP. Their efficiency as INP is depending on supersaturation with respect to ice and ambient temperatures. Aerosol particle types which can act as INP are mainly biological aerosol particles and mineral dust. Biological aerosol particles are active as INP at temperatures above -15 °C. Mineral dust only becomes effective as INP at temperatures of -20 °C and lower but is very common in the atmosphere. Black carbon, organic acids, humic like substances and ammonium sulphate are found to be ineffective at temperatures of heterogeneous ice nucleation (Hoose & Möhler, 2012).

2.3.1 Ice Crystal Shapes

Depending mainly on temperature and supersaturation during the growth period of ice crystals, diverse crystal shapes are formed (Bailey & Hallett, 2009). The shape and size of a falling snow crystal holds important information about its formation process. The crystal shape is depending on temperatures, humidity and turbulence. Complex snowflakes are formed through the aggregation of multiple ice crystals. Round shapes are formed by a process called riming, where water droplets freeze onto the crystal (Maahn et al., 2024). Libbrecht (2008) investigated ice crystal shapes depending on saturation ratio and temperature during formation. The snow crystal morphology diagram, shown in Fig. 2.1, gives an overview of the different crystal shapes, formed under varying temperatures and super-saturations of water. Further explanations considering the snow crystal morphology diagram are given in Libbrecht (2008). Mixed crystal shapes can form, if the environmental conditions alter during the growth phase of the crystal (Fletcher, 2009). Crystal shapes can be investigated using the Video In Situ Snowfall Sensor (see Sect. 3.2.2).

2.4 Processes Influencing Ice Formation

The first important process influencing the ice formation is the Wegener-Bergeron-Findeisen (WBF) process. The “ice crystal theory”, the basis of the WBF process, was described by Wegener (1911), Bergeron (1935) and Findeisen (1938). Wegener, Bergeron and Findeisen discovered, that the water vapour pressure over water is higher than over ice. This leads to the evaporation of water droplets in a cloud in which ice and supercooled water coexist. The water vapour sublimates and leads to the growth of ice crystals (Korolev, 2007).

If the ice crystal grows though the freezing of supercooled water droplets onto the crystal, the process is called riming. Riming is connected with a fast mass gain and a round shape of the crystal. A high water

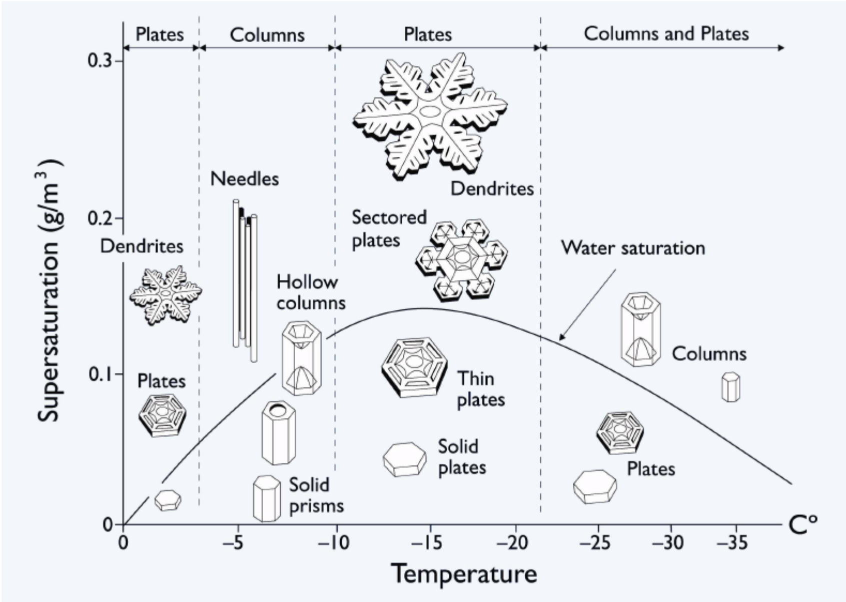

Figure 2.1: Snow crystal morphology diagram (Libbrecht, 2008)

saturation in a cloud is needed for riming (Maahn et al., 2024).

The splintering theory describes the ejection of ice splinters during droplet freezing. When a droplet freezes, the outer layer freezes first, leading to an ice shell formed around the supercooled droplet. The freezing of the inner part of the droplet leads to a pressure rise, forcing the ice shell to break. The breakage leads to the ejection of small ice splinters. These splinters act as INP and therefore increase further ice nucleation in the cloud (Mossop, 1980).

2.5 Cloud Seeding

Cloud seeding is a mechanism which induces glaciation of supercooled cloud droplets in liquid clouds. It creates precipitation by introduction of additional ice nucleating particles (Henneberger et al., 2023). It can occur for natural or anthropogenic reasons.

The natural seeder-feeder mechanism describes the induction of ice nucleation into a low, supercooled, liquid cloud, the so-called feeder cloud by falling ice crystals from a higher seeder cloud (Proske et al., 2021). The falling particle of the seeder cloud grows while passing through the feeder cloud, leading to falling precipitation from the lower feeder cloud (Roe, 2005).

Anthropogenic cloud seeding describes the artificial enforcement of ice nucleation at high subzero temperatures. The procedure was discovered in the mid 1940's. There are two approaches to enforce ice nucleation: the cloud seeding with coolants and the cloud seeding with aerosols. The latter is the most common method. An artificially induced INP population must produce many ice crystals at high subzero temperatures, be easily dispersed and be inexpensive. Vonnegut (1947) found silver iodide and lead iodide especially effective in ice nucleation. Both aerosols are effective as INP at -4 °C in supercooled clouds. Silver iodide (AgI) is known as one of the most active ice nucleating substances. Therefore, it is still used in cloud seeding practices. Small particle sizes are achieved by recondensation from vapor. The silver iodide gets vaporized in a flame within the cloud and condensates due to cooling to environmental temperatures (Götz et al., 1991).

3 Instruments and Methods

The described fundamentals of ice formation can be observed using remote-sensing devices. By sampling air masses, the INP concentration in the air can be analysed. Datasets from both approaches were used in the framework of this thesis.

3.1 Sampling Process

Data from two measurement periods was taken and analysed. The first period covers the days from the 06.01.2024 to 12.01.2024 and the second measurement period from the 26.02.2024 to 01.03.2024. During both time periods a low, supercooled, stratiform Bise cloud formed over the Swiss Plateau. The data from two measurement sites in the Alpine highlands was compared: Eriswil (47.07° N 7.87° E; 740 AMSL) in the Swiss Plateau and Hohenpeißenberg (47.80° N 11.01° E; 780 AMSL) in the south of Germany.

In Hohenpeißenberg and Eriswil air samples were taken by TROPOS and the ETH Zürich respectively using the DPA14 SEQ LVS (DIGITEL Elektronik AG, Volketswil, Switzerland). A flow of 25 litres per minute at ambient temperature and pressure was set. The air flow went through a PM10 inlet. Polycarbonate filters with a pore size of 0.4 µm and a diameter of 47 mm were used. The filters were prepared under a lamiar flow hood by TROPOS. Each filter has been placed in a filter holder cleaned with isopropanol. The filters were stored at –20 °C. In Hohenpeißenberg and Eriswil the first 13 filters were Isopore filters from Merck. From the 13th filter on Nuclepore filters from Whatman were used. A list of filter numbers and corresponding, selected data is given in tables 7.1 and 7.2 in the appendix.

3.2 Instrumentation

The used remote-sensing data was provided by the CLOUDLAB-lll campaign (see Sect. 1). The used instrumentation provided by TROPOS is part of the Leipzig aerosol and cloud remote observations system (LACROS). Various remote-sensing devices of TROPOS were used at the measurement sites, including:

- A lidar ceilometer (Lufft CHM 15k-x) by G. Lufft Mess- und Regeltechnik GmbH
- A Doppler lidar (StreamLine XR+) by HALO Photonics
- A scanning microwave radiometer (RPG-HATPRO-G5) by Radiometer Physics GmbH
- A scanning Doppler cloud radar (METEK MIRA-35) by METEK Meteorologische Messtechnik GmbH
- A precipitation disdrometer (OTT Parsivel²) by OTT Hydromet GmbH
- A multiwavelength Raman polarization lidar (PollyXT) with 13 channels near- field (355 nm, 387 nm, 532 nm, 532 nm cross-pol, 607 nm) and far-field telescope (355 nm, 355 nm cross-pol, 387 nm, 407 nm, 532 nm, 532 nm cross-pol, 607 nm, 1064 nm), manufactured by TROPOS
- and a Doppler non-scanning cloud radar (RPG-FMCW-94-DP) by Radiometer Physics GmbH

3.2.1 Radar and Lidar

Radio and Light Detection and Ranging, radar and lidar respectively, are active ground-based remote-sensing devices. Both devices are emitting pulses of electromagnetic radiation and measuring the signal intensity of backscattered waves (Andrews, 2000). The distance to the scattering event can be inferred from the time delay between emission and reception of the radiation. This relation can be expressed by $z = \frac{1}{2}c \cdot t$ relating to the time as t, the height of scattering as z and the speed of light as c (Andrews, 2000).

A weather radar is using pulses of radiation with wavelengths of 1–10 cm (microwave region). In this region the amount of scattered and absorbed radiation is mostly determined by the existence of precipitating hydrometeors like water drops or ice crystals (Karlsson, 1997). The antenna of the radar is constantly and automatically switching between transmitting and a receiving mode. During the transmitting mode, the antenna is sending a pulse of radiation with a duration in the order of 100 ns. During the longer receiving mode, the antenna is receiving the reflected radiation of the sent pulse (Karlsson, 1997). The number of cycles of transmitting and receiving mode per second is expressed by the Pulse Repetition Frequency (PRF, Karlsson 1997). The strength of the received signal is expressed by the quantity reflectivity factor (unit dBZ), relating the amount of backscattered radiation to the concentration of meteorological targets in the atmosphere (Karlsson, 1997). The radar radiation can be divided into different subregions called radar bands. The choice of a radar band is depending on the meteorological purpose (Karlsson, 1997).

In contrast to the radar, the lidar uses electromagnetic waves in the visible (VIS), ultra-violet (UV), and infrared (IR) regions. In these regions scattering takes place mainly at molecules and aerosols (Andrews, 2000). A laser is used for creating a coherent wave in short pulses with high power at fixed wavelengths (Karlsson, 1997). Using a lidar, the backscatter ratio (R) can be determined, describing the ratio of the total backscatter (molecules and aerosols) to the backscatter from molecules (Andrews, 2000).

Radar and lidar measurements are based on three main principles: atmospheric attenuation, scattering characteristics and propagation conditions. As the atmospheric attenuation must be minimal for measuring backscatter radiation, the wavelengths for measurements are limited to the atmospheric window. The atmospheric window is describing regions of up to 100 % transmittance of radiation in the atmosphere. Therefore, this region of wavelengths is most suitable for backscatter measurements due to the best propagation properties of electromagnetic waves. The choice of the exact wavelength is depending on the size of the target particle. In the VIS region, the attenuation in clean air is low (10^{-1}–10^{-2} dB/km), but high in fog or clouds. This is making lidar suitable for measurements of aerosols and molecules in clean air or below the cloud base. The radar is used for investigations within or above clouds, due to a lower attenuation in condensed or frozen water compared to the VIS radiation (Karlsson, 1997).

For backscatter measurement the Rayleigh and Mie scattering are important. Rayleigh scattering appears, if the target particle is much smaller than the incident wavelength. If the target particle is similar or larger than the incident wavelength, Mie scattering appears (Karlsson, 1997). Therefore, considering Rayleigh scattering is sufficient for radar measurements. Lidar measurements also depend on the more complex Mie scattering in cases of particles larger than the laser wavelength like for example cloud droplets (Andrews, 2000). Details about Rayleigh and Mie scattering are given in Karlsson 1997.

3.2.2 Video in Situ Snowfall Sensor (VISSS)

The Video in Situ Snowfall Sensor (VISSS) is a measuring device for detecting size and shape of individuell snowfall particles. Maximum extent, cross-sectional area, perimeter, complexity and sedimentation velocity are determined. The VISSS consists of two cameras with telecentric lenses for size determination and a LED backlight at the opposite end. Fig. 7.1 shows the setup and a photo of the VISSS (Maahn 2024).

3.2.3 Microwave Radiometer

The used scanning microwave radiometer (RPG-HATPRO-G5) by Radiometer Physics GmbH is a passive humidity and temperature profiler. The radiometer is measuring electromagnetic bands in the microwave region. This region is useful for detecting water molecules in the atmosphere. The radiometer is measuring the brightness temperature of the atmosphere (Foth, 2017). The brightness temperature is the temperature of a black body emitting the same amount of radiation at given wavelengths as the measured object (Meyers, 2002). The radiometer outputs temperature and humidity profiles as well as integrated quantities like the liquid water path (LWP) and the integrated water vapour (IWV). The liquid water path describes the integrated amount of water in the liquid phase in a vertical column of air. The LWP is thus useful for determining the amount of liquid water in clouds.

3.3 Trajectories

Trajectories are used to trace the movement of airmasses or particles over time. Trajectories can be calculated forward (from source location ongoing in time and location) or backwards (from origin to source location and time).

48-hour-trajectories were calculated for Eriswil (47.07° N; 7.87° E) and Hohenpeißenberg (47.80° N; 11.01° E) for 2 am (UTC) and 2 pm (UTC), representing the mid-time of each filter sample period. For Eriswil, backwards trajectories visualize the origin of the air masses. For Hohenpeißenberg, forward trajectories show the movement of air masses after the passage of this research site. The trajectories were calculated for three altitude levels: 100 m, 250 m and 1000 m above ground level. 100 m and 250 m are inside the well-mixed planetary boundary layer (PBL). The well-mixed PBL is representative for the sampled air masses. The height of 1000 m is representative for the free troposphere (above the PBL). The Bise cloud is usually a low cloud, which forms inside the PBL and does not reach the heights above

1000 m (see Sect. 5.1.1). Precipitation data was extracted along the trajectories to evaluate the possible loss of particles bound in precipitation. All trajectories were modulated using the NOAA HYSPLIT model and 0.25° GFS meteorological data (Stein et al., 2015). Note that precipitation data extracted from the trajectories is based on model data and not on actual measurements. Calculated trajectories are shown in Sect. 4.1.2.

3.4 Off-line Immersion Freezing Analysis

Immersion freezing measurements were performed in the Ice Laboratory of TROPOS. The two measurement devices Leipzig Ice Nucleation Array (LINA) and Ice Nucleation Droplet Array (INDA) were used. Both devices are used to investigate the fraction of droplets of a fix volume, frozen at a certain temperature (frozen fraction). From this frozen fraction the INP concentration in the liquid can be calculated (see Sect. 3.4.4).

During the field campaign, air masses got sampled on polycarbonate filters (see Sect. 3.1). The collected filters were handled under a laminar flow hood. A sample suspension from the particles collected on these filters was created using ultrapure (type 1) water. Prior to every measurement day the water quality was checked performing an analysis with INDA. The filter was placed in a 25 ml vial with ultrapure wash water. The vial was placed in an automatic flask shaker at 700 osc/min for 10 minutes.

The created sample suspension was used for the analysis with LINA and INDA (see Sect. 3.4.1 and 3.4.2 respectively).

3.4.1 Leipzig Ice Nucleation Array (LINA)

LINA is a Droplet Freezing Array (DFA) based on the DFA BINARY by Budke and Koop (2015). 90 droplets of 1 µl sample suspension get placed on a hydrophobic glass (see Fig. 3.1). The used cover glass slides of borosilicate glass have a diameter of 40 mm. The glass slides were coated with wax, creating a hydrophobic surface. Droplet interactions like splintering or the Bergeron-Wegener-Findeisen process or droplet evaporation are avoided by individual compartments for each drop and a cover glass slide on top. Used material was cleaned using acetone or ultrasound prior to usage and between samples. The droplet array was cooled down with a rate of 1 K/min. The cooling was performed by a Peltier element inside the freezing stage (LTS120, Linkam Scientific Instruments, Waterfield, UK) and coupled with a cryogenic water circulator (F25-HL, Julabo, Seelbach, Germany). The glass slide is thermally connected to the Peltier element by a thin layer of squalene oil (ACROS Organics, Flair Lawn, NJ, USA). The

Figure 3.1: Leipzig Ice Nucleation Array (LINA) at TROPOS with partly frozen droplets during sample suspension freezing analysis (Foto: Anja Marie Hardt)

detection of droplet freezing is based on the illumination of the droplets and a detecting camera system. The droplets are illuminated by a shadow free LED dome lightning (SDL-10-WT, MBJ-Imaging GmbH, Hamburg, Germany). A charge-coupled camera takes an image every 6 seconds. The image sequence describes a resolution of 0.1 K temperature difference in each frame. The illumination creates a ring-shaped reflection in the liquid droplets, which vanishes with freezing of a droplet. This appearance can be analysed by image evaluation using a Python algorithm (M. Hartmann & Simon, 2024).

3.4.2 Ice Nucleation Droplet Array (INDA)

INDA is a DFA based on the same principle than LINA but using a different droplet volume. 50 µl drops of sample suspension are placed in 96 wells of a PCR plate (Brand GmbH & Co.KG, Wertheim, Germany). Sample suspensions of two filters were evaluated using one PCR plate. This concludes to 48 wells of sample suspension per filter. The PCR plate was sealed with a transparent foil, disabling droplet interactions. INDA consists of an ethanol bath, a thermostat (FP45-HL, Julabo, Seelbach, Germany) and a metal PCR holder. The PCR plate is placed in the ethanol bath using the PCR holder (see Fig. 3.2). The ethanol level exceeds the liquid level of the drops in the PCR plate. The ethanol bath is cooled down with a rate of 1 K/min. The PCR plate is illuminated from below. A camera is recording images from above with a frequency of one frame every 0.1 K. A droplet freezing results in more light being absorbed and a dark spot in the resulting image. The images were analysed using image evaluation in Python (M. Hartmann & Simon, 2024).

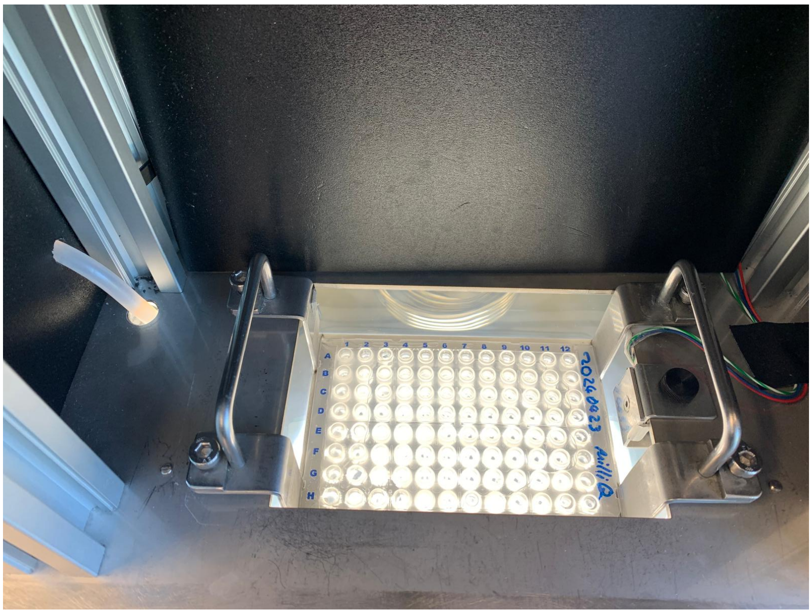

Figure 3.2: PCR plate in Ice Nucleation Droplet Array (INDA) at TROPOS during water freezing analysis (Foto: Anja Marie Hardt)

3.4.3 Heat-labile Fraction

For determining the heat-labile fraction of INP in the sample suspension, the PCR plates used for INDA were heated. The sample suspension was heated up to 90 °C for 30 minutes. The heat labile fraction of INP was destroyed and therefore ineffective in ice nucleation. After the heating process the INDA analysis was performed again.

3.4.4 INP Calculation

The analysis delivered a fraction of droplets of sample suspension, frozen at a certain temperature ($N_{\text{frozen}}(T)$). This frozen fraction (f_{ice}) can be used to calculate the concentration of INP in the air volume which was sampled on the filter (see Eq. 3.1).

$$f_{\text{ice}} = \frac{N_{\text{frozen}}(T)}{N_{\text{drop}}} \tag{3.1}$$

First, the wash water volume needs to be calculated, which was used for creating the sample suspension. The final wash water volume ($V\text{wash}_{\text{final}}$) was calculated by the wash water used for the LINA measurement ($V\text{wash}_{\text{LINA}}$), the wash water used for the INDA measurement ($V\text{wash}_{\text{INDA}}$) and the leftover Volume (V_{leftover}) after the LINA measurement. The wash water calculation is given by the following equation (M. Hartmann & Simon, 2024).

$$V_{\text{wash}_{\text{final}}} = \frac{V_{\text{wash}_{\text{LINA}}} \cdot (V_{\text{leftover}} + V_{\text{wash}_{\text{INDA}}})}{V_{\text{leftover}}} \tag{3.2}$$

For the standard procedure 3000 µl were added and 100 µl were used for the LINA measurement. The wash water volume for LINA is 3000 µl. To the leftover volume of 2900 µl 3500 µl were added for the INDA measurement. Using equation 3.2 the final wash water volume for INDA was calculated to $V_{\text{wash}_{\text{final}}} \approx$ 6620 µl. Using the frozen fraction (see Eq. 3.1), the drop volume of LINA and INDA (V_{drop})and the wash water volume (V_{wash}) for LINA and INDA, the concentration of INP ($cINP$) in the filtered air volume (V_{air}) can be calculated as follows (Eq. 3.3, Vali, 1971). The drop volume of LINA is 1 µl and the drop volume of INDA is 50 µl.

$$cINP = -\ln(1 - f_{\text{ice}}) / \left(\frac{V_{\text{air}} \cdot V_{\text{drop}}}{V_{\text{wash}}} \right) \tag{3.3}$$

The calculated concentration of INP in dependence of the temperature is shown in the results chapter (see Sect. 5.2.1). The calculated INP concentration is presented using a logarithmic scale. The confidence interval shown in the result chapter is based on the uncertainty concerning the Poisson distribution of INP in the droplets. Following the example of previous, similar research like Sze (2023) or Gong (2022), the total error is not considering statistical or systematic errors from the sample preparation or the measurement devices. Considering these errors in this thesis is unrewarding due to the limited number of samples. The confidence interval is calculated using equation 3.4, referring to the number of drops used in the measurement as n_{drop} and the fraction of frozen drops as f_{ice} (Agresti & Coull, 1998). The number of drops used during the LINA measurement is 90 and during the INDA measurement 48.

$$\text{Confidence interval} = \left(f_{\text{ice}} + \frac{1.96^2}{2 \cdot n_{\text{drop}}} \pm 1.96 \cdot \sqrt{\frac{f_{\text{ice}} \cdot (1 - f_{\text{ice}}) + \frac{1.96^2}{4 \cdot n_{\text{drop}}}}{n_{\text{drop}}}} \right) / \left(1 + \frac{1.96^2}{n_{\text{drop}}} \right) \tag{3.4}$$

4 Results

In the following chapter the results of the INP analysis of the air samples taken in Eriswil and Hohenpeißenberg are presented. The results are presented in the context of selected remote-sensing data and trajectories.

4.1 Remote-Sensing and Trajectories

A selection of remote-sensing data and calculated trajectories are shown in the following sections. The selection is based on the relevance for the interpretation of the filter sample analysis. Additional remote-sensing data and calculated trajectories are presented in the appendix. The results of the following remote-sensing devices will be presented for both measurement periods (6.1.24–12.1.24 and 26.2.24–1.3.24): RPG94 radar, HATPRO radiometer and VISSS. Lidar results are presented in Figs. 7.6 and 7.7 in the appendix due to high signal attenuation by the low-level clouds and therefore limited informative value.

The temperature series taken by the HATPRO Radiometer in Eriswil is presented in Fig. 4.1 and Fig. 4.2 for the first and second measurement period respectively. A temperature series for Hohenpeißenberg is shown in Fig. 4.4. The RPG94 radar reflectivity factor (Ze) of the first and second measurement period is presented in Fig. 4.5 and Fig. 4.6, respectively. The liquid water path (LWP) of the HATPRO radiometer is presented in Figs. 4.7 and Fig. 4.8.

Selected VISSS images are presented in Figs. 4.9 to 4.13. All VISSS images for both measurement periods are presented in the appendix.

In Figs. 4.14 and 4.15 only the backward trajectories for Eriswil in cases of northeast winds are presented. For reasons of overview the trajectories of the first and second measurement period will be presented separately. Additional calculated trajectories are presented in Figs. 7.14, 7.15, 7.16, and 7.17 in the appendix. The first measurement period is referring to the sampling time from the 6th of January 2024 to the 12th of January 2024. Selected backward trajectories for Eriswil calculated for this time period are

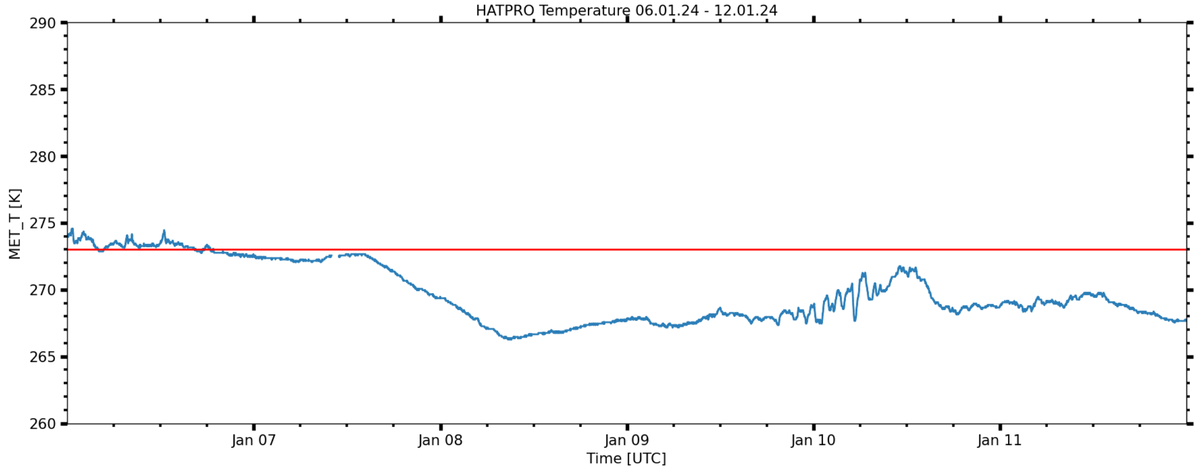

Figure 4.1: Temperature at ground level of the HATPRO microwave radiometer in Eriswil from the 6th of January to the 12th of January 2024 with 0 °C line shown in red.

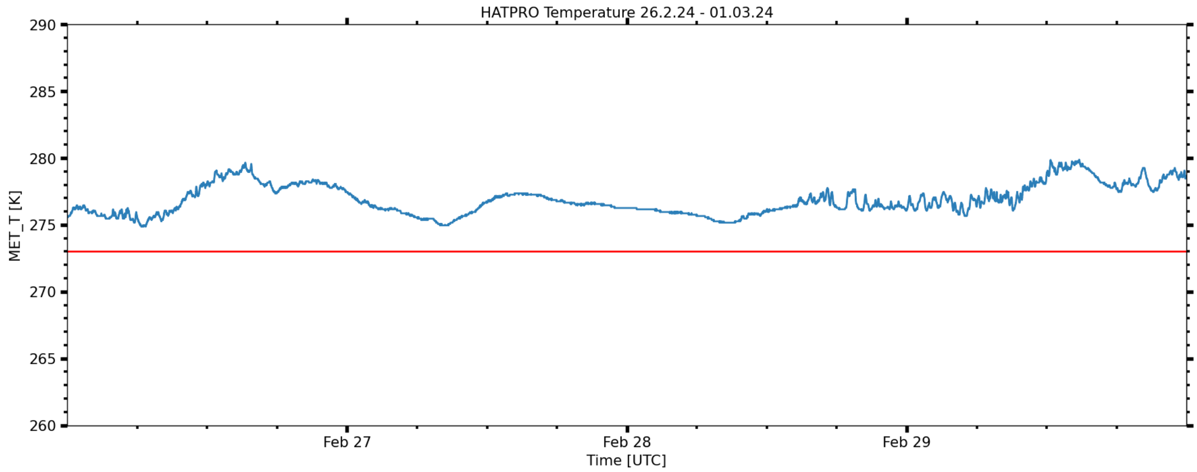

Figure 4.2: Temperature at ground level of the HATPRO microwave radiometer in Eriswil from the 26th of February to the 1st of March 2024 with 0 °C line shown in red.

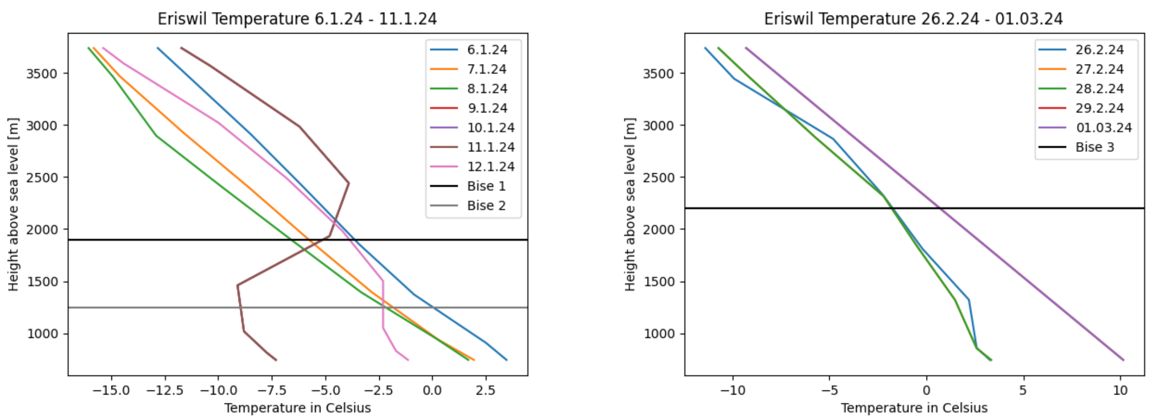

Figure 4.3: Vertical temperature profile from model calculations for Eriswil from the 6th of January to the 12th of January 2024 and from the 26th of February to the 1st of March, showing the cloud top height of the Bise clouds in black and grey.

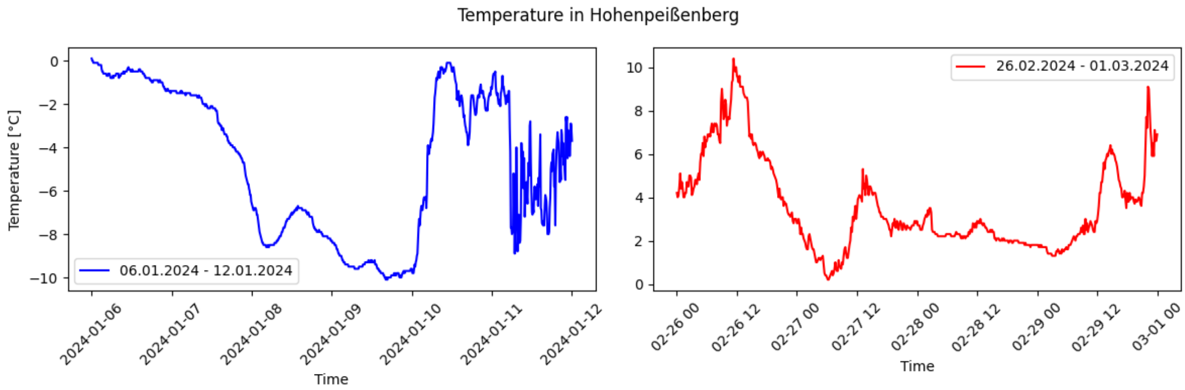

Figure 4.4: Temperature at 2 m above ground in Hohenpeißenberg from the 6th of January to the 12th of January 2024 (data: Climate Data Center 2024).

presented in Fig. 4.14. The second measurement period is referring to the sampling time from the 26th of February 2024 to the 1st of March 2024. Selected Backward trajectories for Eriswil calculated for this time period are presented in Fig. 4.15.

4.2 Filter Sample Analysis

As the temperatures during the first and the second measurement period differ decisively, they will be presented separately (see Figs. 4.1 and 4.2). The first measurement period is referring to the sample time from the 6th of January 2024 to the 12th of January 2024. INP data of the first measurement period is presented in Fig. 4.16 and Fig. 4.17 for Eriswil and in Fig. 4.18 and 4.19 for Hohenpeißenberg.
The second measurement period is referring to the sample time from the 26th of February 2024 to the 1st of March 2024. INP data for this sampling period is shown in Figs. 4.20 and 4.21 for Eriswil and Figs. 4.22 and 4.23 for Hohenpeißenberg. Additional INP data in presented in Figs. 7.19, 7.20 and 7.21 in the appendix.

Due to the high uncertainty, the first frozen drop (lowest INP concentration) of INDA and heated measurements has been removed in all INP plots. For the overlapping INP concentrations of LINA and INDA, the first 5 frozen drops of LINA have been removed for the sake of readability, due to a higher uncertainty compared to the INDA concentrations. The uncertainty of all data is represented by the confidence interval. INDA and LINA data is represented by the same colour code for enhanced visibility of contrasts between Hohenpeißenberg and Eriswil data. The given dates and times in the plot titles of the INP analysis are referring to the end time of the 12-hour sampling period in Eriswil (ERI) and Hohenpeißenberg (HPB). Therefore, these dates and times are referring to the release time of the filter from the sampler. An overview of all start and end times of the filter samples is presented in tables 7.1 and 7.2 in the appendix.

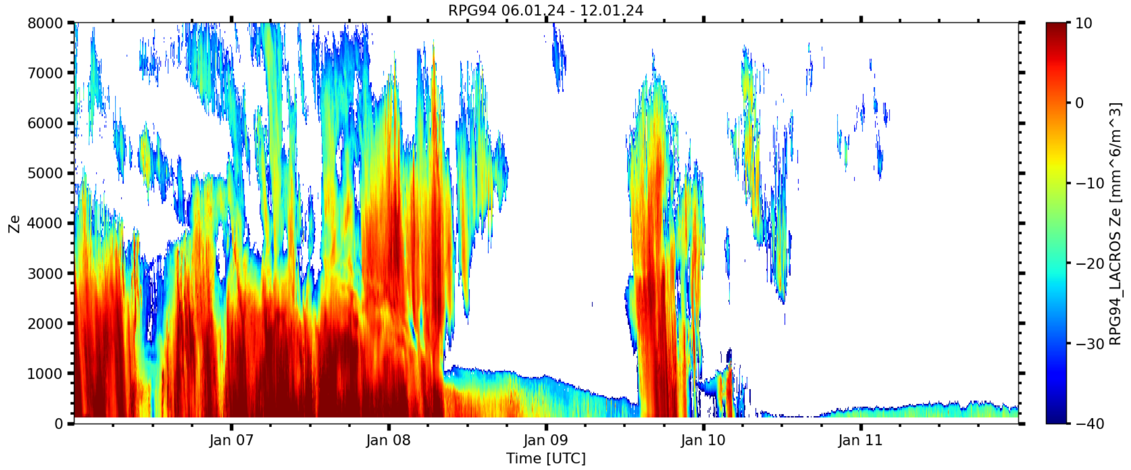

Figure 4.5: RPG94 Radar reflectivity factor (Ze) in Eriswil from the 6th of January to the 12th of January 2024.

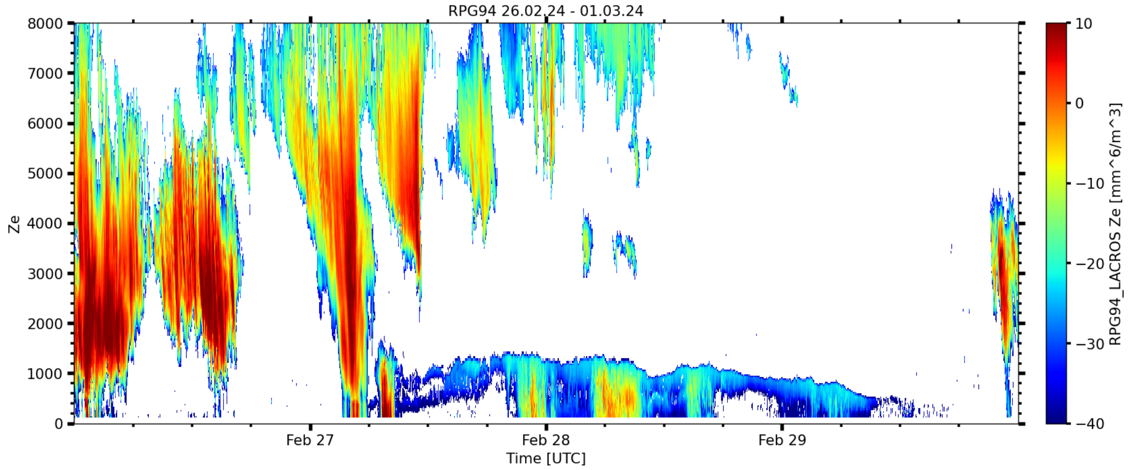

Figure 4.6: RPG94 Radar reflectivity factor (Ze) in Eriswil from the 26th of February to the 1st of March 2024.

4.3 Comparison Plots

Figs. 4.24 and 4.25 show a combined plot of INP data for Eriswil and Hohenpeißenberg respectively, for evaluation of differences between the two measurement periods.

Figs. 4.26 and 4.27 show a comparison of INP data for filters with and without seeding activity in Eriswil.

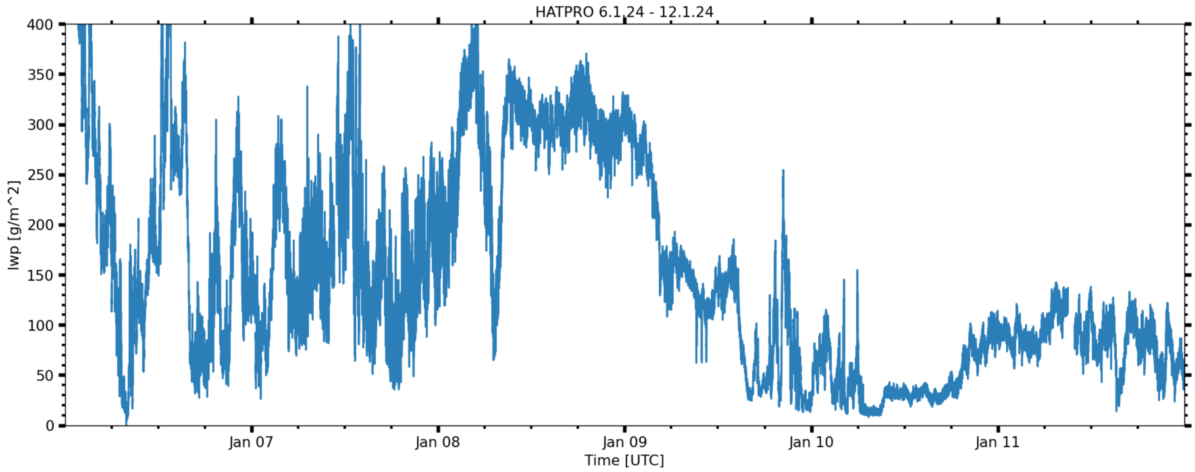

Figure 4.7: LWP of the HATPRO Radiometer in Eriswil from the 6th of January to the 12th of January 2024.

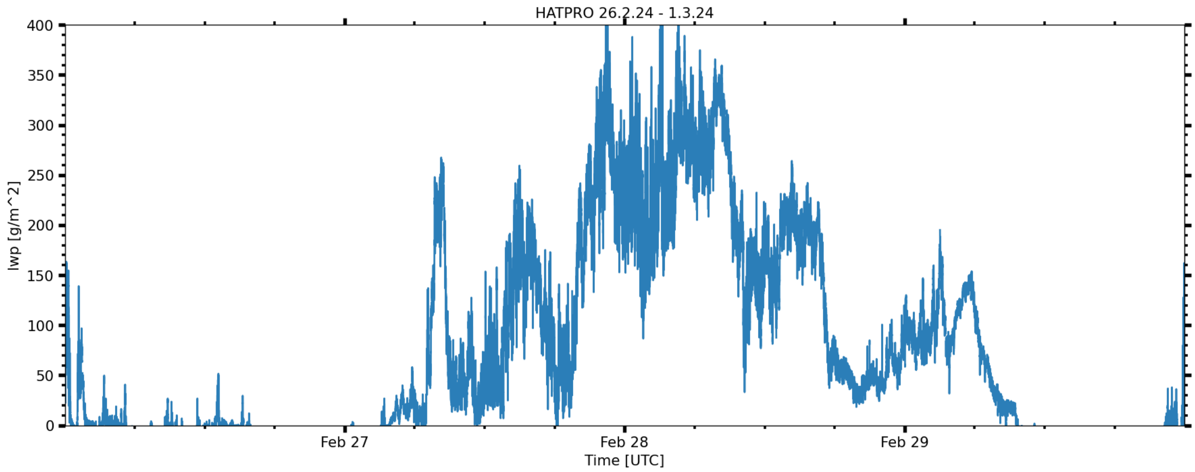

Figure 4.8: LWP of the HATPRO Radiometer in Eriswil from the 26th of February to the 1st of March 2024.

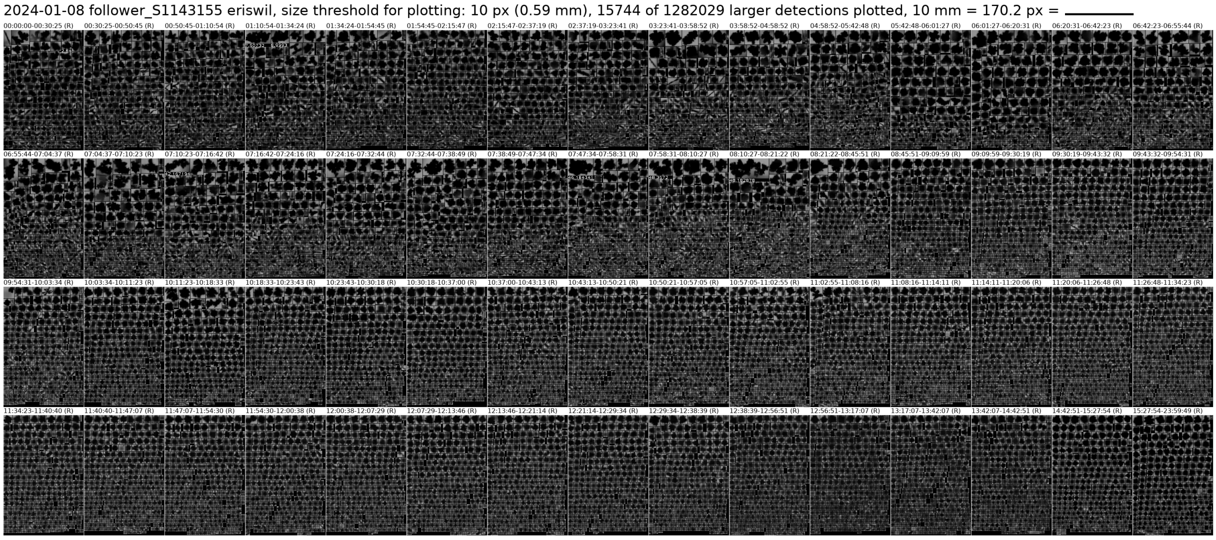

Figure 4.9: VISSS images from the 8th of January 2024 in Eriswil.

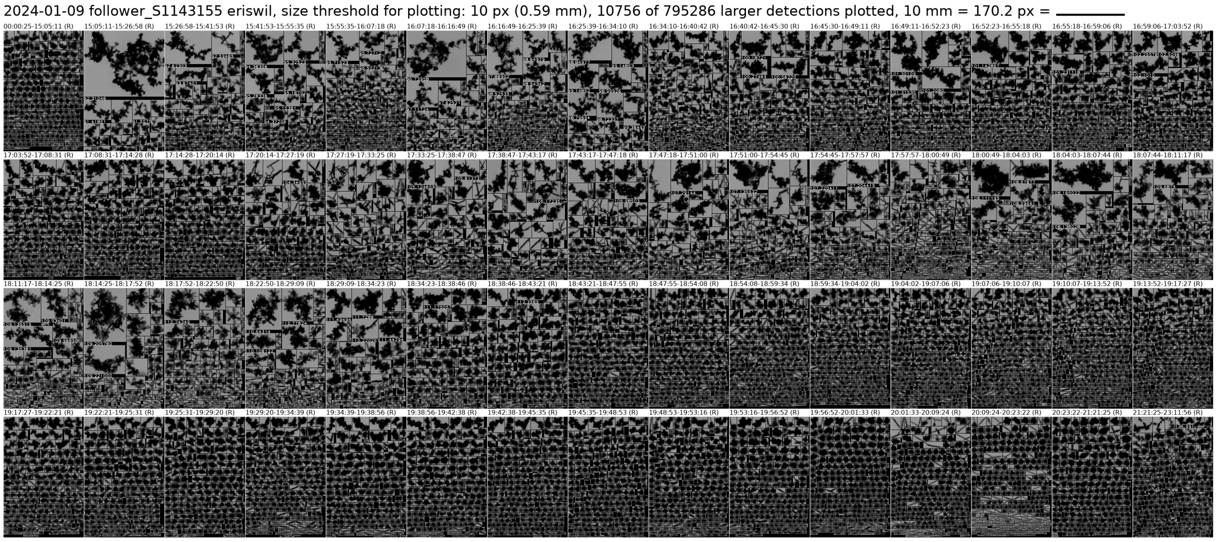

Figure 4.10: VISSS images from the 9th of January 2024 in Eriswil.

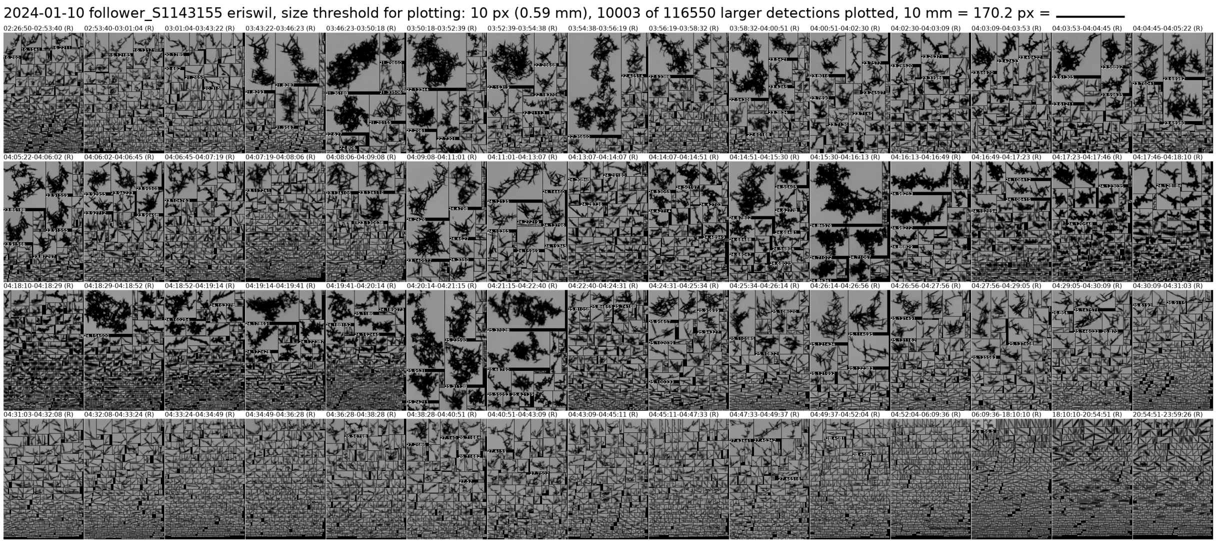

Figure 4.11: VISSS images from the 10th of January 2024 in Eriswil.

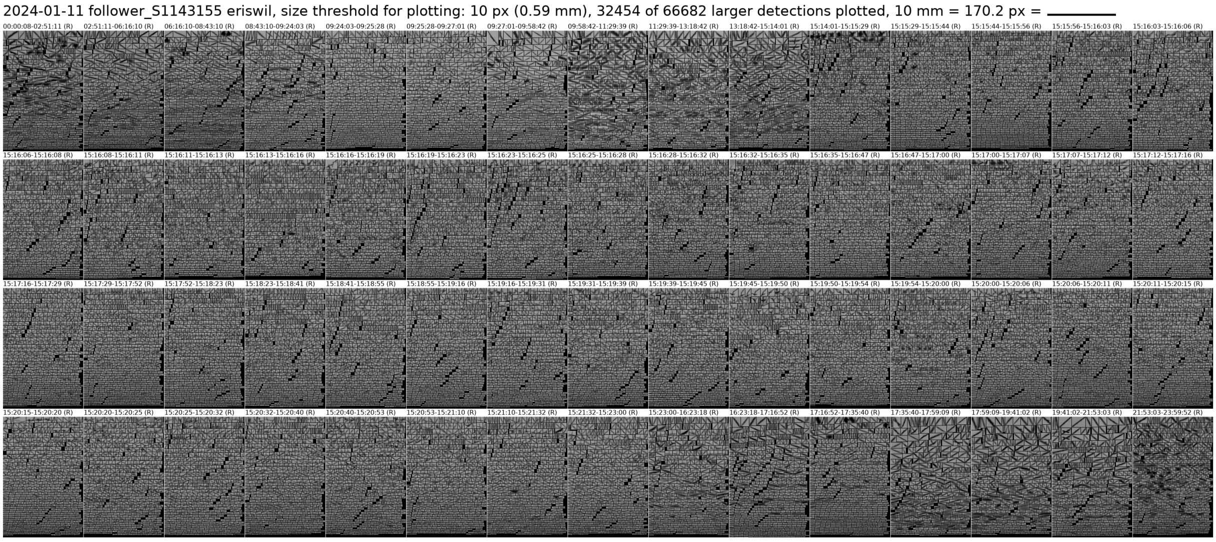

Figure 4.12: VISSS images from the 11th of January 2024 in Eriswil.

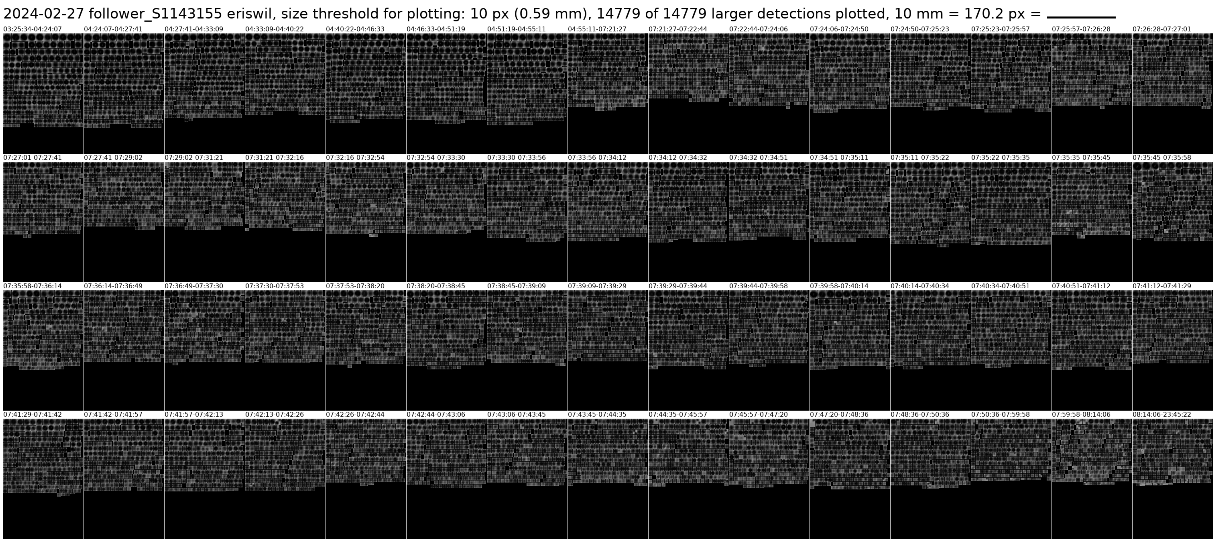

Figure 4.13: VISSS images from the 27th of February 2024 in Eriswil.

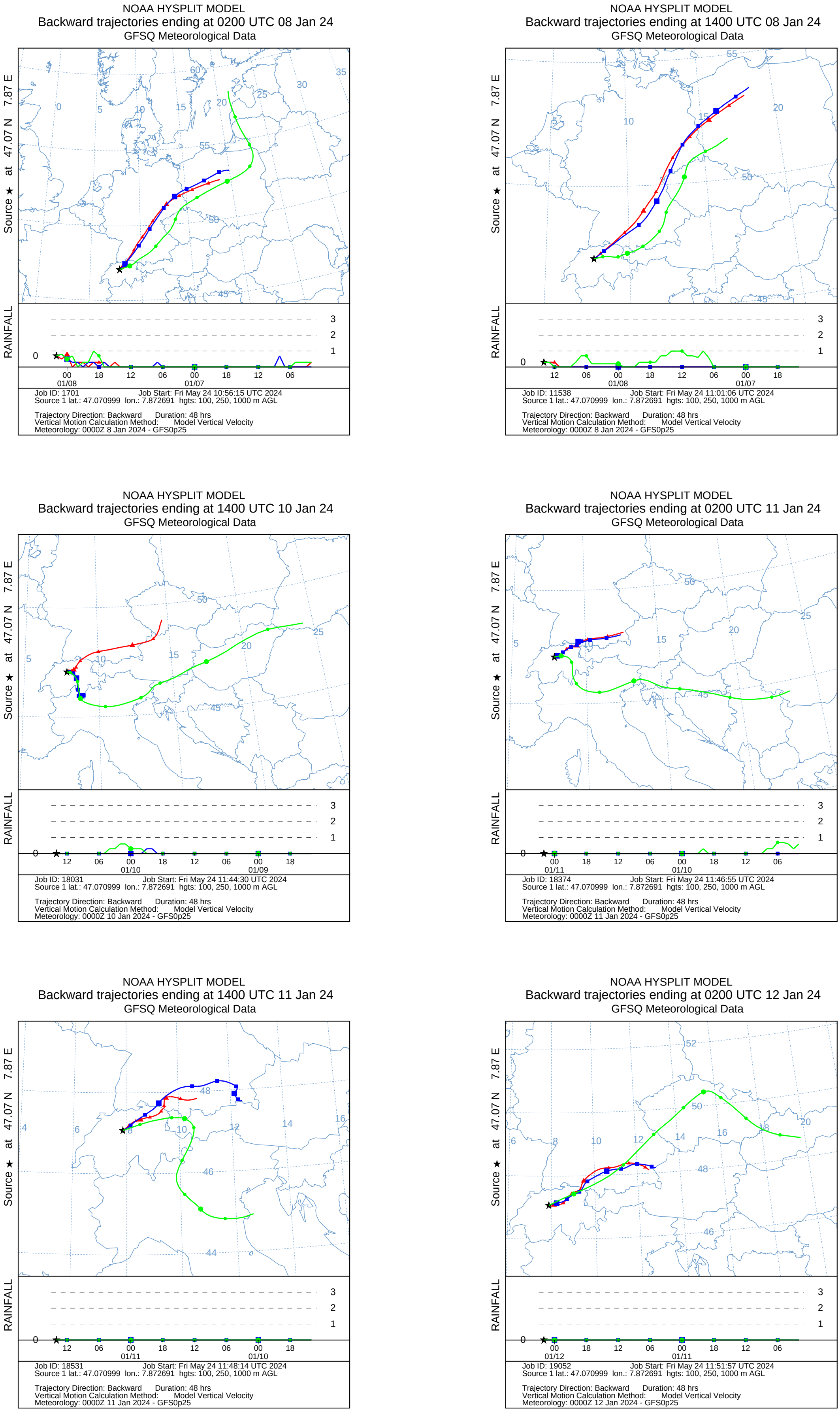

Figure 4.14: Selected backward trajectories from Eriswil within the first measurement period including model precipitation data.(Model: Stein 2015)

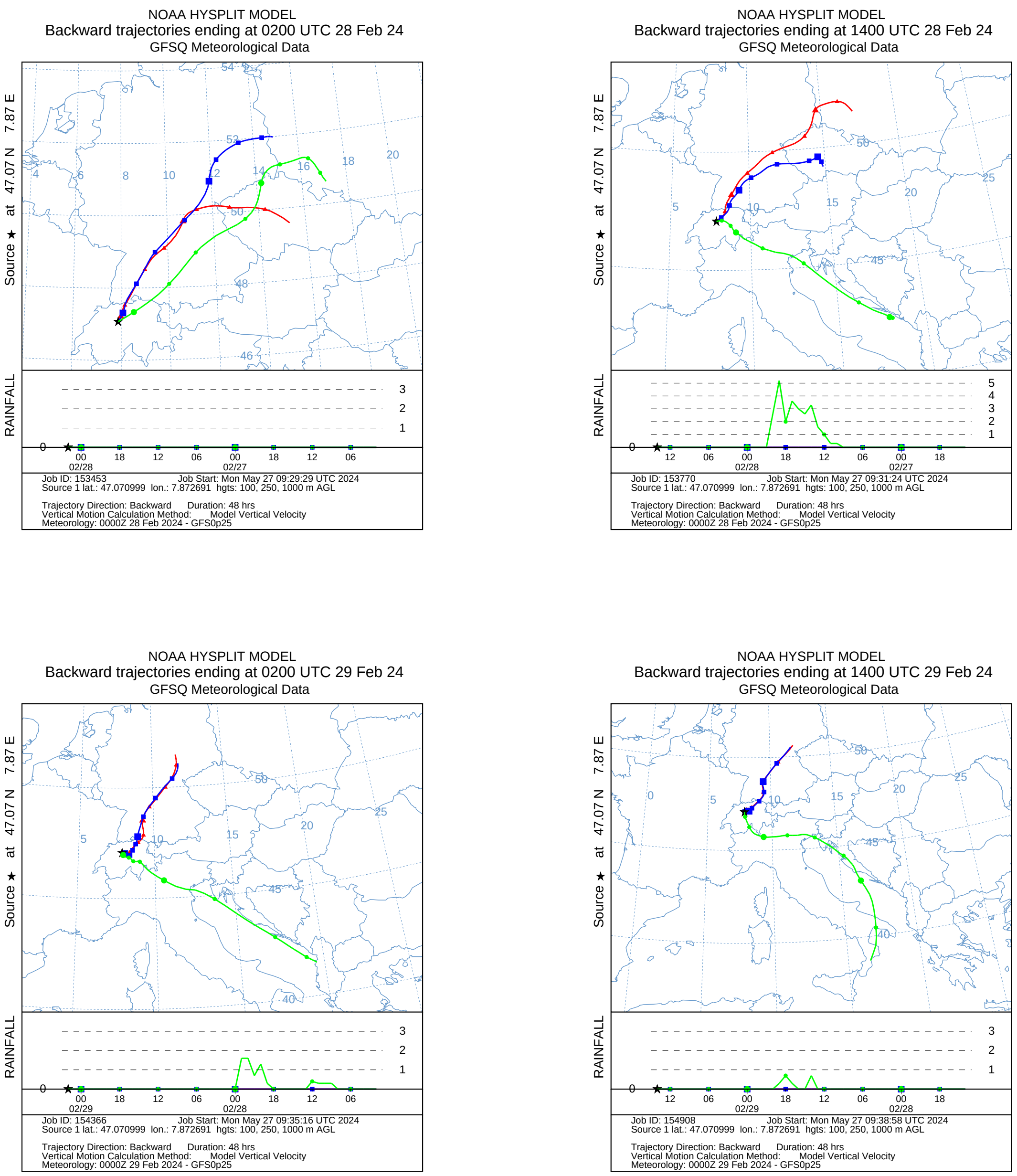

Figure 4.15: Selected backward trajectories from Eriswil within the second measurement period including model precipitation data. (Model: Stein 2015)

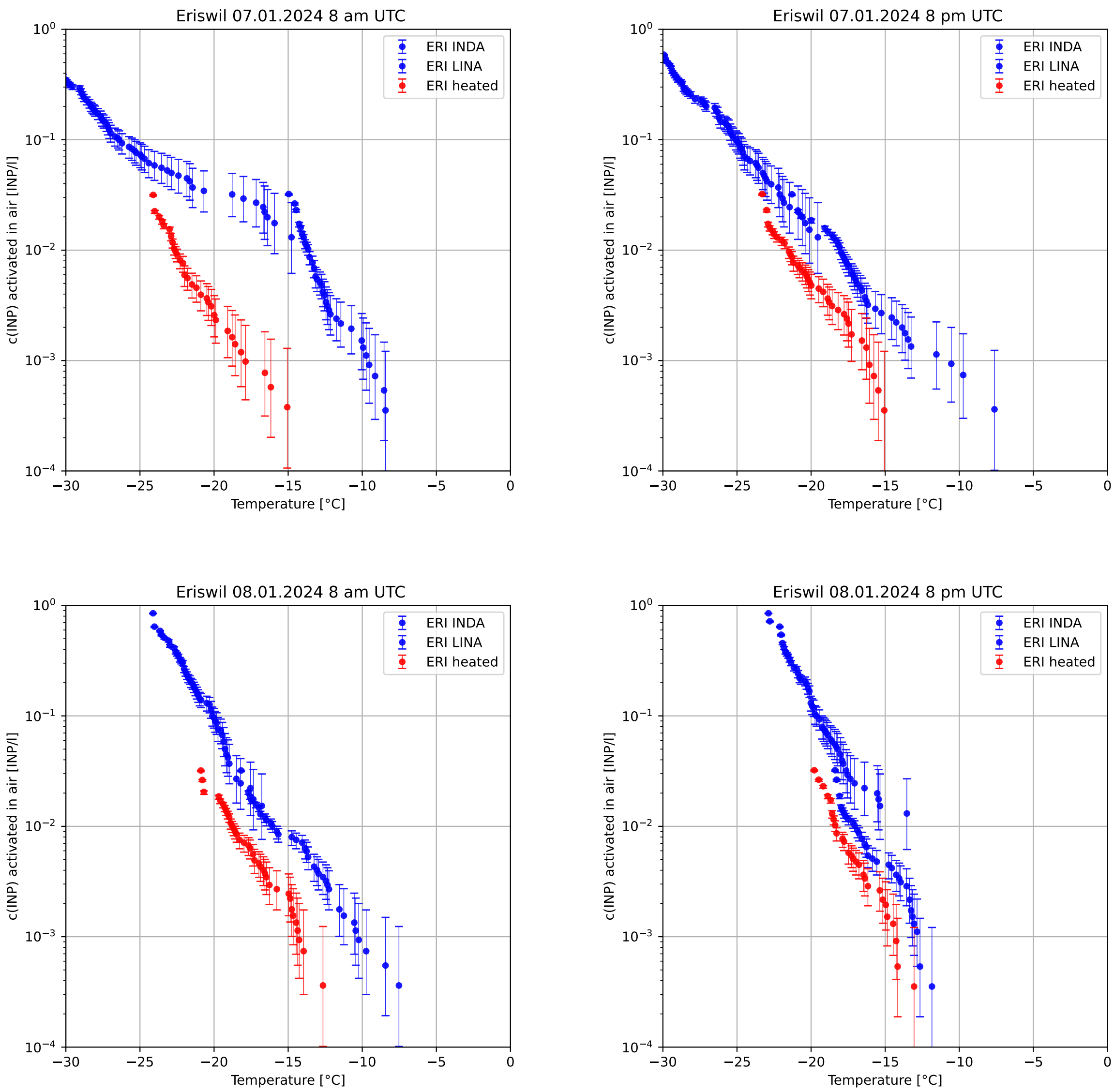

Figure 4.16: INP data for filters from the 6th of January to the 8th of January 2024 in Eriswil. Results from the freezing analysis using INDA and LINA (blue) as well as the INDA results for heated PCR plates (red).

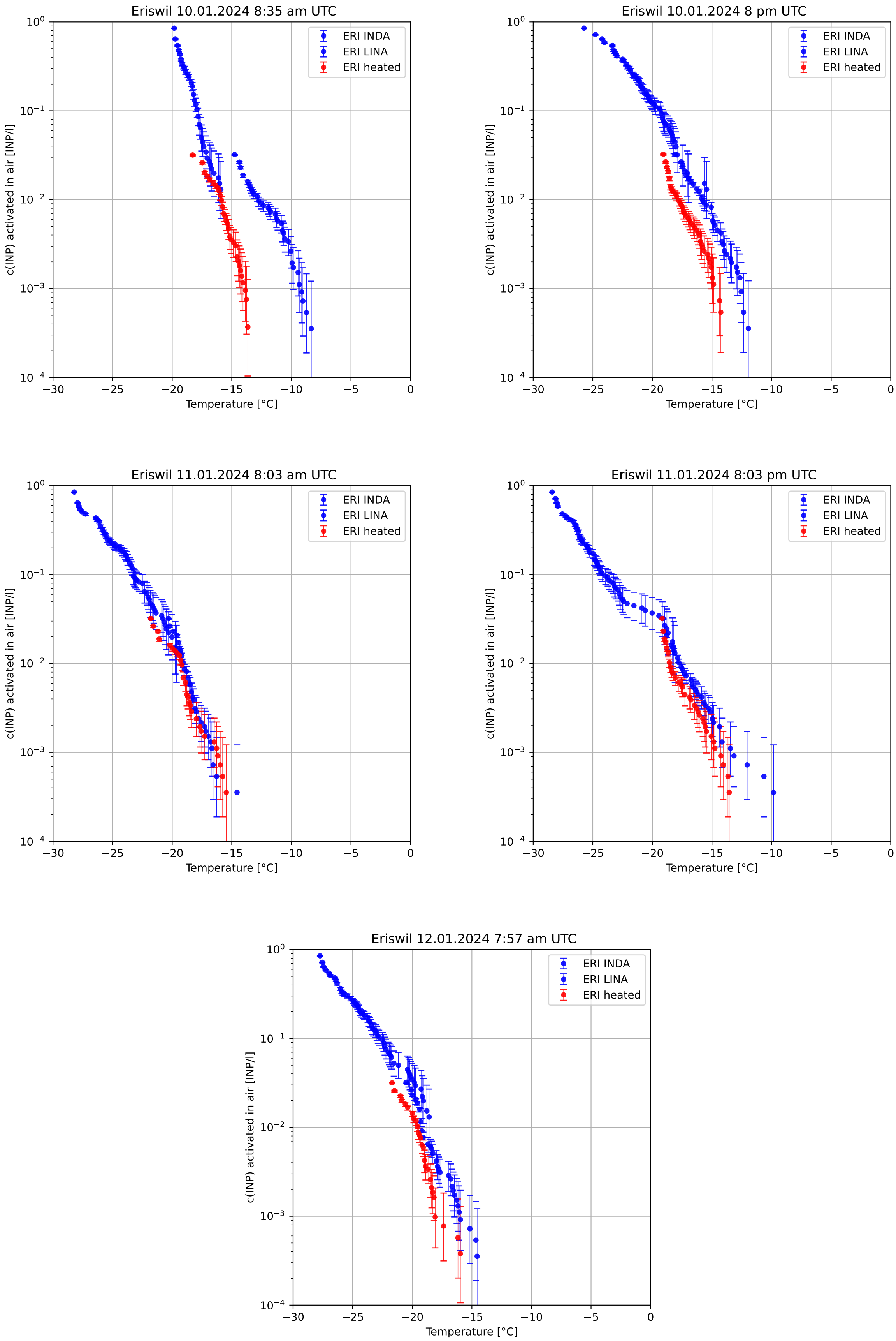

Figure 4.17: INP data for filters from the 10th of January to the 12th of January 2024 in Eriswil. Results from the freezing analysis using INDA and LINA (blue) as well as the INDA results for heated PCR plates (red).

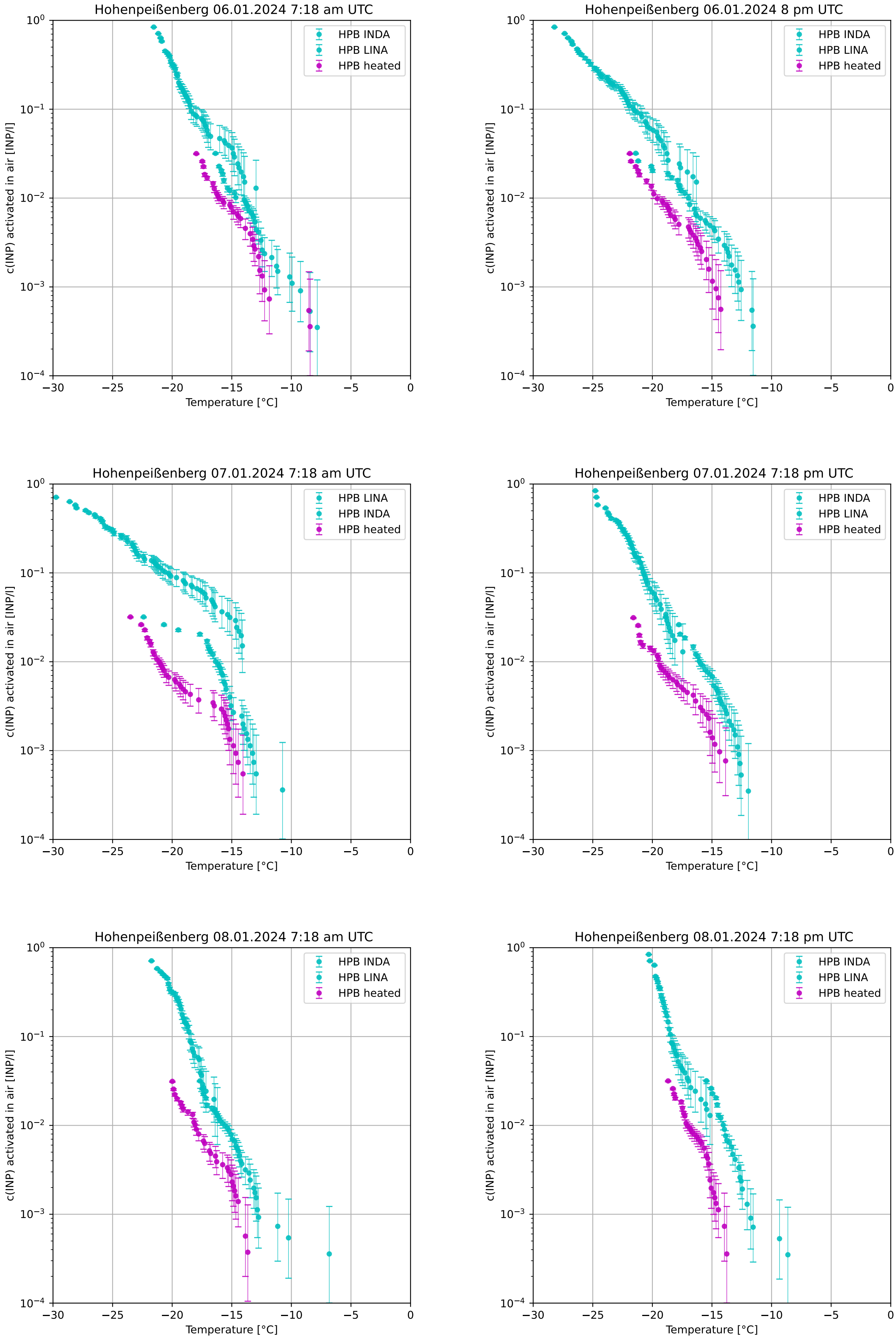

Figure 4.18: INP data for filters from the 6th of January to the 8th of January 2024 in Hohenpeißenberg. Results from the freezing analysis using INDA and LINA (cyan) as well as the INDA results for heated PCR plates (magenta).

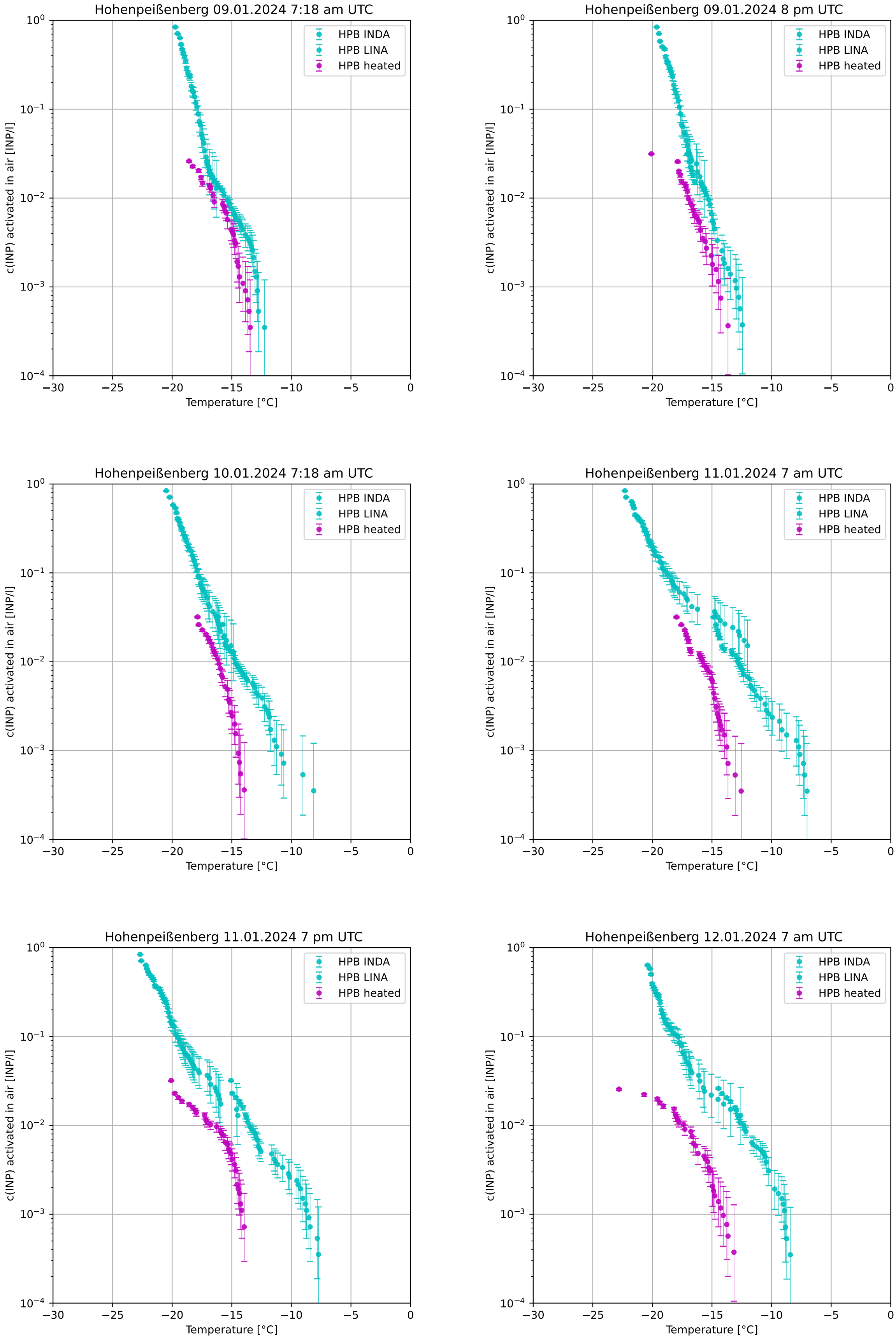

Figure 4.19: INP data for filters from the 9th of January to the 12th of January 2024 in Hohenpeißenberg. Results from the freezing analysis using INDA and LINA (cyan) as well as the INDA results for heated PCR plates (magenta).

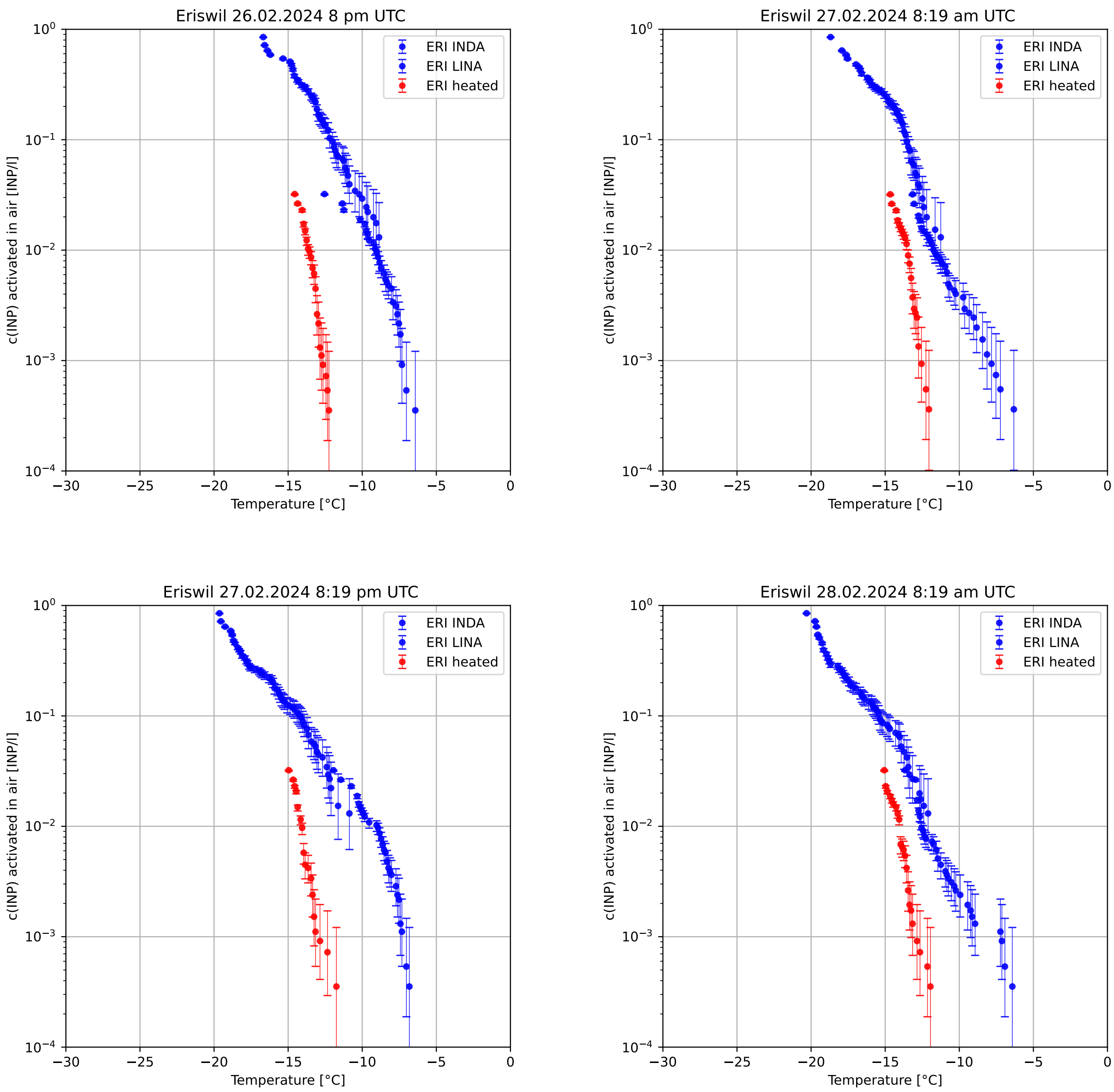

Figure 4.20: INP data for filters from the 26th of February to the 28th of February 2024 in Eriswil. Results from the freezing analysis using INDA and LINA (blue) as well as the INDA results for heated PCR plates (red).

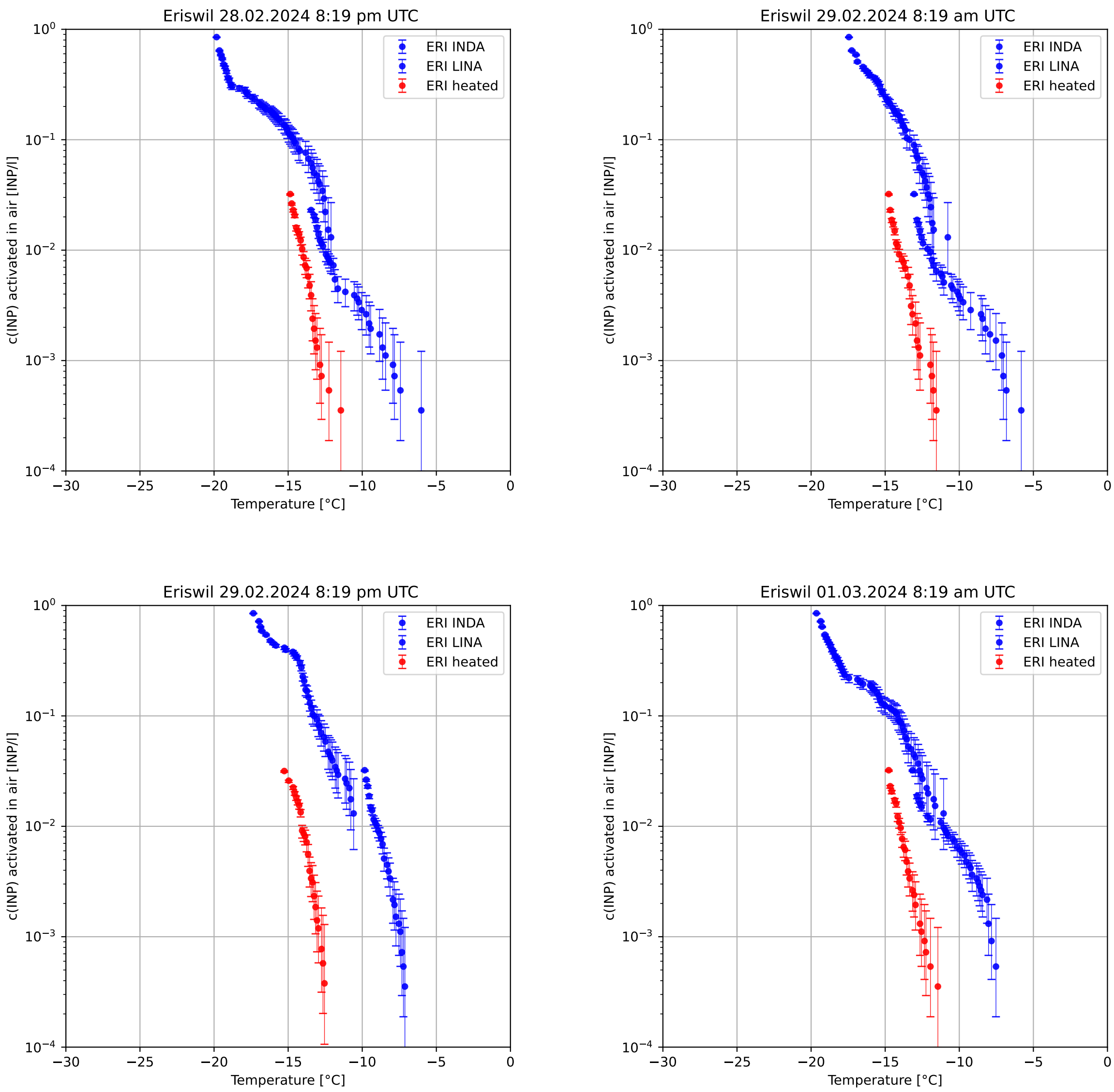

Figure 4.21: INP data for filters from the 28th of February to the 1st of March 2024 in Eriswil. Results from the freezing analysis using INDA and LINA (blue) as well as the INDA results for heated PCR plates (red).

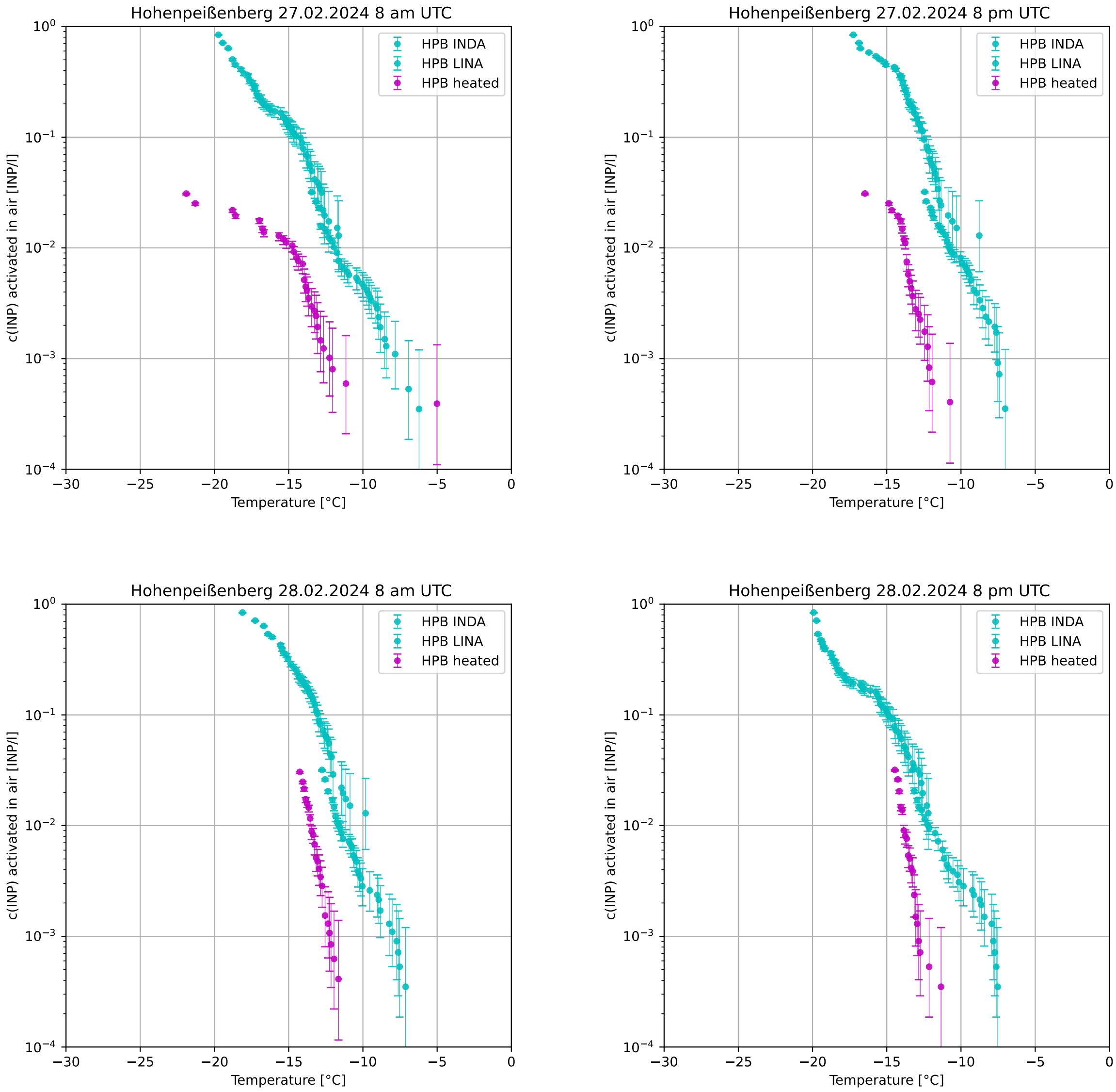

Figure 4.22: INP data for filters from the 27th of February to the 28th of February 2024 in Hohenpeißenberg. Results from the freezing analysis using INDA and LINA (cyan) as well as the INDA results for heated PCR plates (magenta).

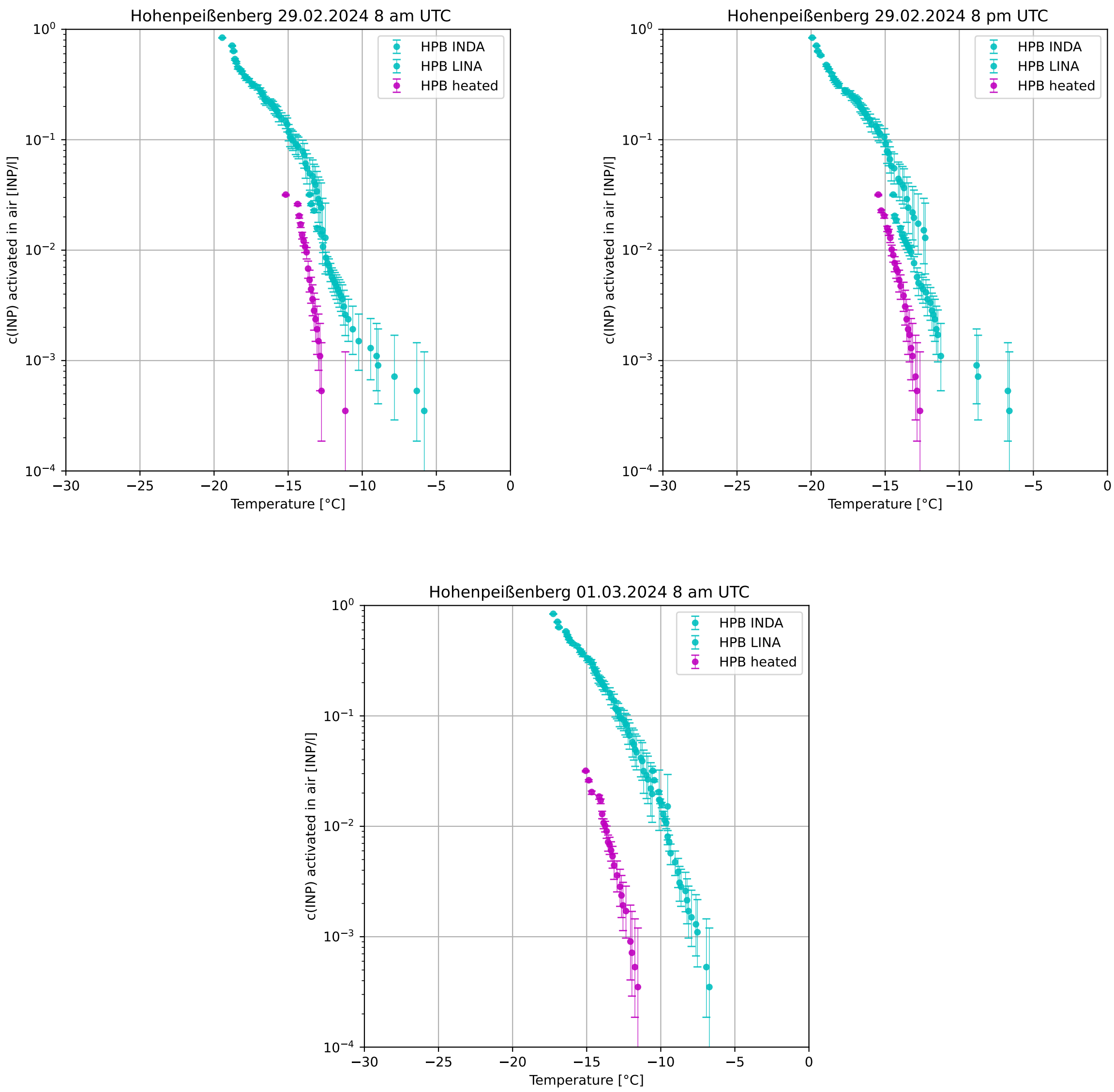

Figure 4.23: INP data for filters from the 29th of February to the 1st of March 2024 in Hohenpeißenberg. Results from the freezing analysis using INDA and LINA (cyan) as well as the INDA results for heated PCR plates (magenta).

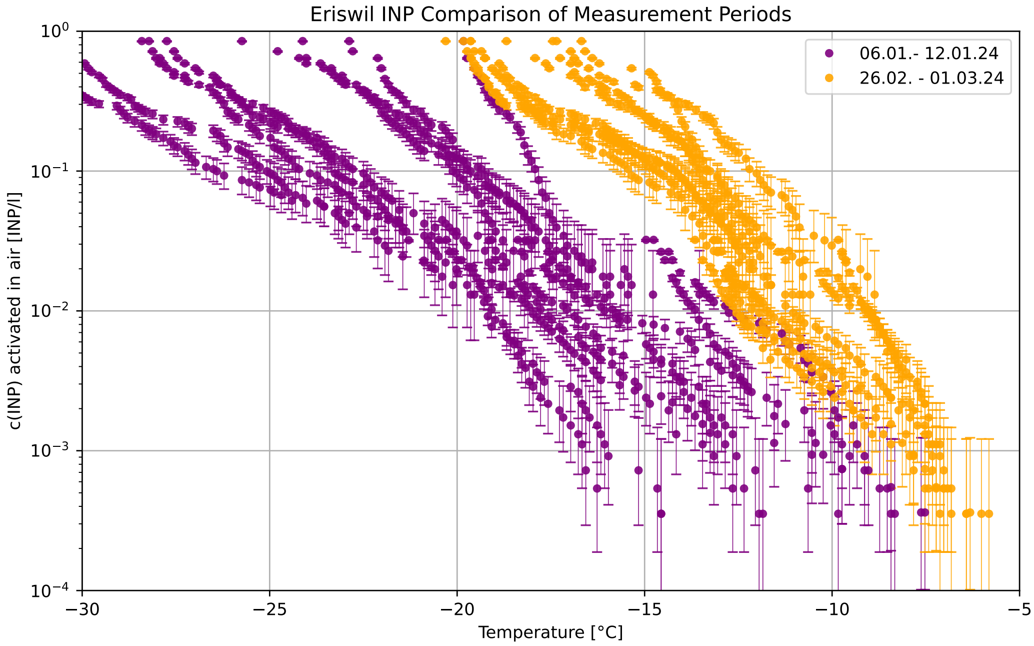

Figure 4.24: Comparison of INP data for Eriswil between the two measurement periods from the 6th to 12th of January 2024 and the 26th February to the 1st of March 2024. Showing the first Measurement period in purple and the second measurement period in orange.

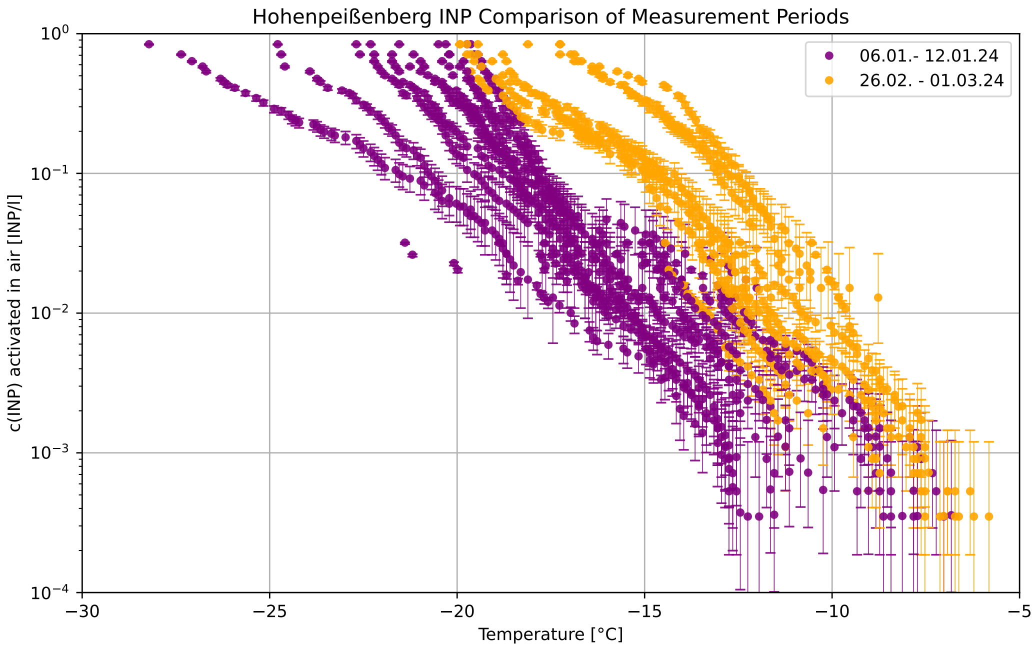

Figure 4.25: Comparison of INP data for Hohenpeißenberg between the two measurement periods from the 6th to 12th of January 2024 and the 26th February to the 1st of March 2024. Showing the first Measurement period in purple and the second measurement period in orange.

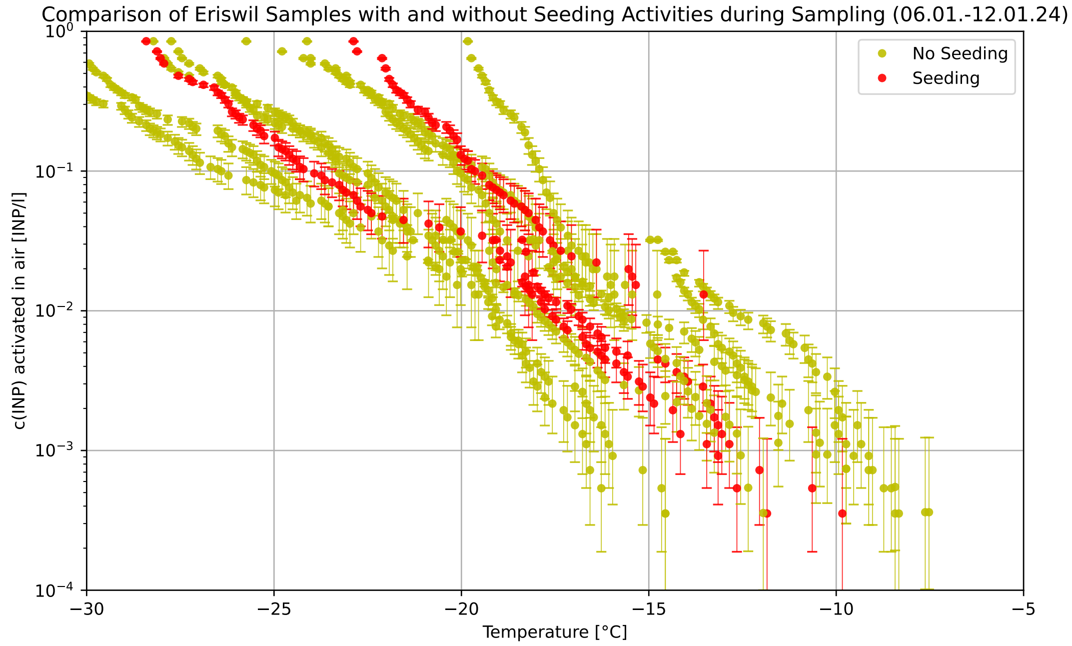

Figure 4.26: Comparison plot of INP data for filters with (yellow) and without (red) seeding activity in Eriswil during the first measurement period.

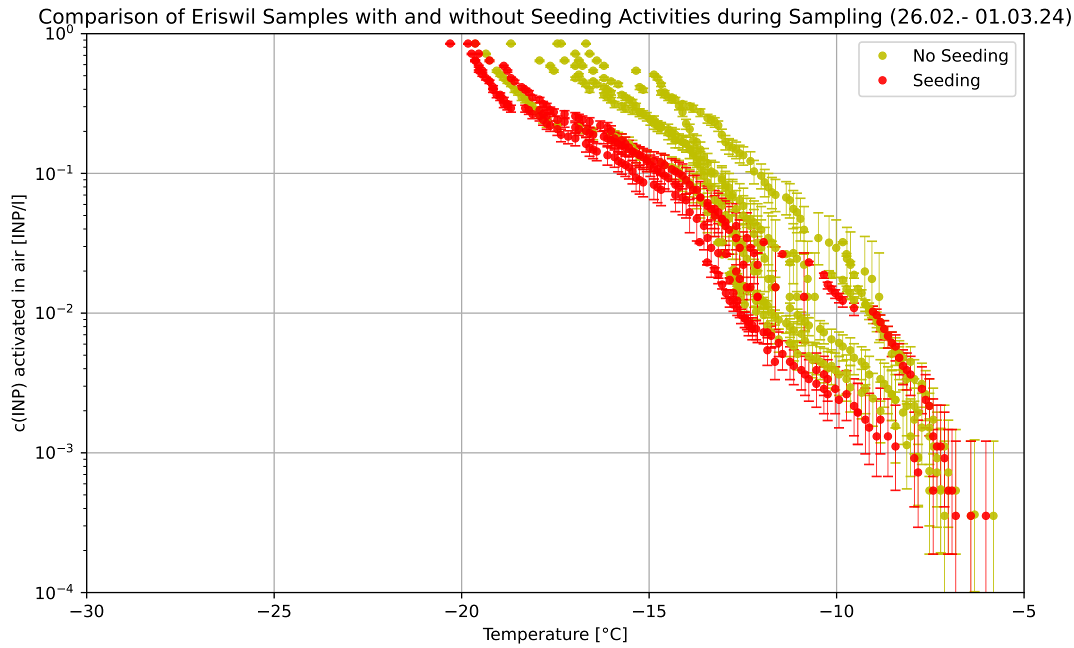

Figure 4.27: Comparison plot of INP data for filters with (yellow) and without (red) seeding activity in Eriswil during the second measurement period.

5 Discussion

In the following chapter the presented results from chapter 4 are interpreted and connected with each other.

5.1 Interpretation of Remote-sensing Results

5.1.1 RPG Result & Temperature Interpretation

Figs. 4.5 and 4.6 show the backscatter values (radar reflectivity factor) of the RPG94 radar situated at the measurement site in Eriswil. Fig. 4.5 is showing the results for the first measurement period. Fig. 4.6 is showing the results for the second measurement period. In both plots the cloud height for each day and the cloud cover can be seen. In both measurement periods there was a continuous low-cloud cover over Eriswil. A radar plot showing the stratiform cloud in detail is presented in Figs. 7.4 and 7.5 in the appendix.

The first low stratiform cloud (Bise 1) was formed on the 8th of January around 9 am and did last until the 9th of January around 15 pm. This cloud reached a maximum height of around 1150 m above ground level. The second low stratiform cloud (Bise 2) was formed on the 10th of January around 9 am and did last until the end of the measurement period on the 12th of January. This cloud reached a maximum height of around 500 m above ground level. The third low stratiform cloud (Bise 3) was formed on the 27th of February at around 9 am and did last until the 29th of February around 12 noon. This cloud reached a maximum height of around 1450 m above ground level.

The temperatures during the first measurement period were constantly lower than in the second period (see Figs. 4.1 and 4.2). From the 7th to the 12th of January the temperatures in Eriswil were constantly below 0 °C (see Fig. 4.1). The temperatures during the second measurement period were above 0 °C during the whole time period (see Fig. 4.2). The temperatures during the first Bise cloud reached around –7 °C on the 8th of January. Temperatures during the second Bise cloud reached a minimum value of

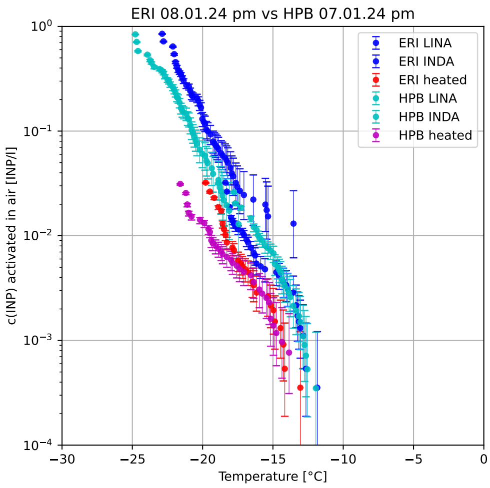

(a)

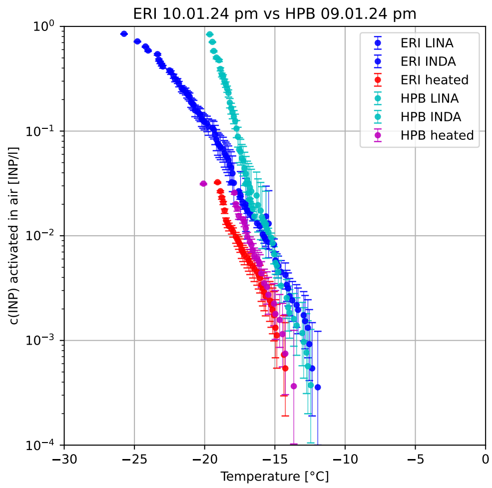

(b)

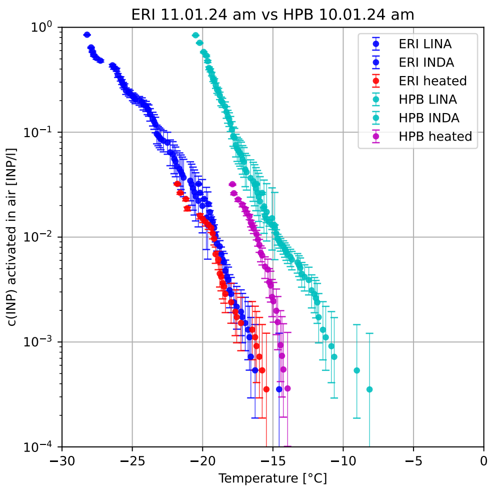

(c)

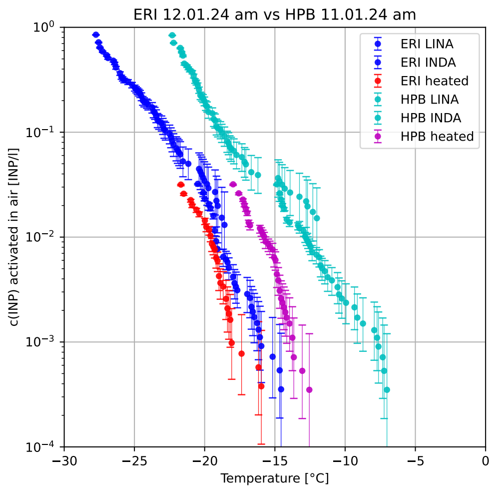

(d)

Figure 5.1: INP comparison of Eriswil and Hohenpeißenberg with 24 hour time differences within the first measurement period.

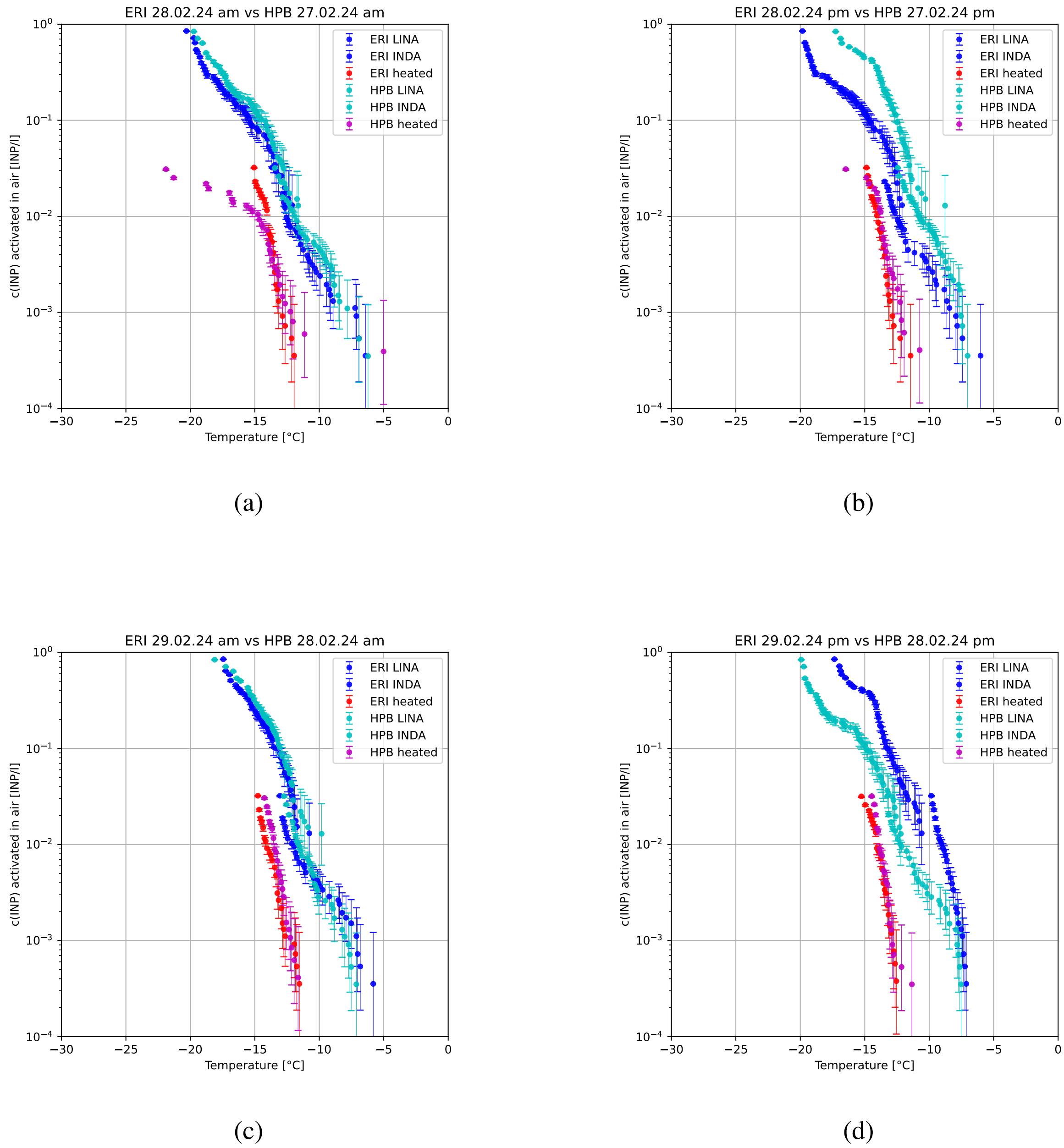

(a) (b) (c) (d)

Figure 5.2: INP comparison of Eriswil and Hohenpeißenberg with 24 hour time differences within the second measurement period.

around –9 °C at the 11th of January. The third Bise cloud in the second measurement period was formed in presence of higher temperatures, with minima around –2 °C at the 26th and 28th of February. It has to be noted that the temperature model has limited accuracy. The real temperature values can vary from the model values, especially in presence of temperature inversions, which are difficult for the model to simulate. The model temperature data is missing for the 9th and 10th of January as well as for the 27th and 29th of February.

From the 6th of January until the 7th of January around 12 noon, the cloud cover was continously present up to around 4000 m above ground. Additional disconnected alto cumulus and cirrus clouds are present above the base cloud. Between the two Bise periods there is a cloud reaching up to around 7000 m from the 9th of January 12 noon until the 10th of January. During the second Bise period there are single cirrus clouds visible. The cloud base during the first measurement period is constantly very low and reaches the lower detection limit height of the RPG94 cloud radar. The lidar observations in Fig. 7.6 in the appendix also indicates that the Bise cloud is reaching ground levels, as the signal attenuation is very high.
During the second measurement period, the cloud base is varying strongly from values close to the ground during the Bise cloud and in the morning of the 26th of February, up to 6000 m in the evening of the 26th (see 4.6). Clouds of large extension in height exist at the 26th of February and in the morning of the 27th. From the morning of the 27th on the low Bise cloud develops. Parallel to this, clouds disconnected from the Bise exist at higher levels of the atmosphere until noon of the 28th. At the night from the 28th to the 29th cirrus clouds are visible in the RPG94 cloud radar observations. The lidar observations (Fig. 7.7) shows the difference between the high cloud base at the 26th, where lidar observations are showing the cloud base attenuation and the Bise period with no visible data due to high attenuation near the ground. This indicates the Bise cloud to reach to ground.

5.1.2 LWP Interpretation

The microwave radiometer results presented in Figs. 4.7 and 4.8 are showing the LWP during both measurement periods. The LWP in the first period shown in Fig. 4.7 until the first Bise cloud at the 8th of January is alternating strongly. This is due to high cloud variability, allowing liquid water masses at lower heights as well as ice in higher heights and falling precipitation (see Fig. 7.2), removing liquid water from the cloud. The first Bise cloud (Bise 1) is way lower than the cloud height at the 6th and 7th of January. The LWP is stable during the first Bise at high levels of about $300\ \mathrm{gm}^{-2}$. In the evening of the 8th of January precipitation occured, leading to a dropping of the LWP and a lower cloud height of the Bise 1. Parts of the liquid water were consumed by the ice crystals falling through the layer. For example due to riming or Wegener-Bergeron-Findeisen effect. The high cloud in between Bise 1 and Bise 2 is connected with lower levels of LWP than the Bise 1 despite a cloud height of up to around 7000 m above ground. The high cloud top leads to very low temperatures in the cloud, allowing ice formation. Little amounts of precipitation are falling from this cloud. The existence of ice in the cloud is lowering the LWP due to higher amounts of cloudwater in the solid and less in the liquid state. During the formation and the expansion of Bise 2 the LWP is growing simultaneously with the cloud height of the Bise, indicating the Bise cloud to consist mainly of liquid water and the cirrus clouds at high heights to consist of ice. Little amounts of precipitation are detected in the afternoon of the 11th of January (see Fig. 7.2).

The LWP of the second measurement period is shown in Fig. 4.8. The LWP values are low until the morning of the 27th of February 2024. This indicates all clouds at the 26th of February and the morning of the 27th of February with large extensions in height to consist mainly of ice. Despite the ice clouds there are only little amounts of detected precipitation during the whole second measurement period (see Fig. 7.3). The LWP is showing simultaneous values to the extensions of the Bise cloud existing from around 9am on the 27th until around 12 noon on the 29th. This indicates the Bise cloud to contain large amounts of liquid water.

5.1.3 VISSS Data Interpretation

The VISSS data is useful for detecting falling ice crystals also in cases of very little amounts. The results of the VISSS are showing the presence of ice crystals during the entire first measurement period. During the period from the 6th to 7th of January a mixture of snowflakes and ice needles is detected (see Figs. 7.8 and 7.9). On the 8th of January there are thicker and rounder hydrometeor shapes detected during the whole day (see Fig. 4.9). Very little amounts are falling between 3 pm and midnight this day. The rounder shapes indicate a riming process, which is possible due to the high content of liquid water in the Bise cloud. The higher amounts of detected crystals until 3 pm could be explained by crystals falling from the higher cloud above, which grow in the Bise cloud due to the high liquid water content while falling. This process was possibly enhanced through the splintering effect, causing further crystals to form. This also explains the shrinking of the cloud above to a small extension until 3 pm.

On the 9th of January there is a mixture of snowflakes, ice needles and rounder crystal shapes detected (see Fig. 4.10). Very little amounts are falling from midnight to 3 pm. Higher amounts are falling from 3 pm to midnight, which is in accordance with the end of the Bise cloud and the beginning of the high reaching cloud in the evening of 9th of January.

On the 10th of January the crystal shapes are dominated by needles and thin snowflakes with single snowflake aggregates (see Fig. 4.11). Small amounts are detected throughout the whole day with especially few crystals from 9 pm to midnight. This is in accordance with the existence of a larger cloud above the very thin Bise cloud until the evening of the 10th of January.

The crystal shapes on the 11th of January are dominated by ice needles. Main amounts on that day are falling between 15 and 15:30 UTC. There is no VISSS data for the 12th of January.

During the second measurement period there are single round ice crystals detected for the 26th of February (see Fig. 7.10). These crystals are falling from the high reaching clouds before the Bise formation, containing a high amount of ice according to the LWP values discussed earlier.

Round crystal shapes are detected on the 27th of February from 3:30 to 5 am and from 7:20 to 8:15 am (see Fig. 4.13). This is in coherence with the existence of a high-reaching cloud coloumn that extended from the ground to heights exceeding 8000 m (see Fig. 4.6). On the 28th and the 29th of February there are no falling ice crystals detected in Eriswil (see Figs. 7.11 and 7.12).

5.2 INP Data and Trajectory Evaluation

In the following the analysed air samples from Eriswil and Hohenpeißenberg are compared to each other. The comparability of the two sampling places is checked by the interpretation of the calculated trajectories.

Mentioned times and dates of the INP data are referring to a time period of 12 hours before the sample time which is represented in the title of each INP plot. The results for heated and non-heated samples are presented. The contrast between activated INP in the heated versus the non-heated sample is referred to as heat labile fraction of INP. As biological INP are heat labile and active at higher temperatures, the heat labile fraction is interpreted as biological fraction of INP.

5.2.1 Evaluation for Eriswil

Fig. 4.16 shows the INP concentration in air masses over Eriswil from the 6th of January to the 8th of January in 12-hour time steps within the first measurement period.

The INP curve of the 7th of January in the upper two images of Fig. 4.16 is showing a strong heat lability. The origin of air masses in PBL heights for this day are northwest according to calculated trajectories. The amount of activated INP above temperatures of –10 °C is lower than on the 6th of January. The INP curve of the heated sample is still showing a strong contrast to the total activated INP curve from the

8 am sample of this day. This is indicating a high percentage of biological INP origin in northwestern air masses. While the contrast between the heated and non-heated INP curve is strong for all measured INP concentrations in the first sample of the 7th of January, the contrast in the second sample of this day is less pronounced for concentrations higher than about 10^{-3} INP/l. The INP curve for concentrations larger than 10^{-2} INP/l is very flat for the first sample of this day. Since this is concerning exclusively the LINA measurement, a measurement error has to be considered.

Results of the freezing analysis for samples taken on the 8th of January in Eriswil are shown in the last two images of Fig. 4.16. The origin of air masses from within the PBL for this day according to calculated trajectories is north-east. The sample time of the second sample of this day, matches the time of formation of Bise 1. The gap between the INP curve of the heated sample and the non-heated sample is small in the first sample of this day. It nearly vanishes in the second sample. This is indicating a small amount of biological INP in air masses of north-eastern origin and a very low percentage of biological INP during the existence of the Bise cloud on that day.

The results of the freezing analysis for the 10th to 12th of January in Eriswil are shown in Fig. 4.17. According to the trajectories, the air masses within the PBL for the first sample of the 10th of January, shown in the first plot of this figure are originating from the south. The origin of the air for the second sample of this day is split into the different heights. Only for the lowest height of 100 m the air is of north-eastern origin. For the other heights the air is originating from the southeast. On the 11th and 12th of January the origin of air is northeast. A Bise cloud over Eriswil was formed from the time of the second sample of the 10th of January on.

The first sample of the 10th of January is showing a high fraction of activated INP at temperatures above –10 °C. Up to about $5 \cdot 10^{-3}$ INP/l are activated above –10 °C. The INP curve of the heated sample is showing a visible contrast to the total activated INP curve. This contrast is visible for all measured INP concentrations of the heated sample. This indicates a biological fraction of INP in southern air masses. The contrast between activated INP from the heated and non-heated samples is getting smaller in the second sample of the 10th of January. This is indicating a lower percentage of biological INP than in the first sample of this day.

For the first samples from the 11th and 12th of January there is no relevant contrast between the INP curve of the heated and non-heated samples. In the samples of this time period, the first INP are activated at very low values around –15 °C. The small contrast between heated and non heated INP for the second sample of the 11th of January is only concerning INP concentrations below about 10^{-3} INP/l.

This supports the observation from Fig. 4.16 of an irrelevant biological fraction in activated INP in the air during the existence of a Bise cloud over Eriswil. Due to the small or missing biological fraction in INP, the total INP are getting activated at lower temperatures in samples taken during the existence of a Bise cloud over Eriswil.

Figs. 4.20 and 4.21 show the results for samples taken during the second measurement period in Eriswil. All shown samples from the evening of the 26th of February to the morning of the 1st of March in Eriswil show high activation temperatures for INP as well as a large biological fraction. A large fraction of INP is activated above –10 °C. This can be explained by the positive temperatures existing during the second measurement period in Eriswil (see Fig. 4.2). The high temperatures hinder the activation of INP and therefore the loss from the air during transport. The high temperatures also accelerate biological activity which leads to a higher production of biological INP. This INP could also be added to the air masses in Eriswil or during transport, potentially even between Hohenpeißenberg and Eriswil.

Samples taken on the 6th of January in Eriswil show an untypically high INP activation for atmospheric samples. Since the filters layed on top of all other filters a pollution during transport or storage is possible. The photo of the prepared filters of Eriswil shown in the appendix (Fig. 7.18) additionally shows a crack in the case of filter 2. The results of these filters are shown in Fig. 7.19 in the appendix. Due to technical problems during the sampling process in Eriswil and Hohenpeißenberg, filter samples from the 9th of January in Eriswil are missing.

5.2.2 Evaluation for Hohenpeißenberg

Fig. 4.18 is showing the freezing analysis results of individual days during the first measurement period in Hohenpeißenberg.

For the whole time period from the 6th to the 12th of January 2024 the activation temperatures of INP in the heated samples taken in Hohenpeißenberg are nearly constant. Only the first sample taken at the 6th of January is showing slightly higher freezing temperatures of the heated sample for the lowest two INP points (see first plot in Fig. 4.18). As these two data points are placed with an unusual distance to the higher INP points, a measurement error has to be considered. The quite constant INP activation temperatures in the heated samples of Hohenpeißenberg are starting from temperatures of about –13 °C to –14 °C on. The heat labile fraction of activated INP is small for samples from the 6th and 7th of January. For both samples from the 8th of January there is a slightly higher heat labile fraction in activated INP for concentrations lower than 10^{-3} INP/l. This concentration in INP is low compared to other samples from Eriswil and Hohenpeißenberg with a relevant heat labile fraction in activated INP.

For both samples from the 9th of January shown in the first two plots of Fig. 4.19 the heat labile fraction in activated INP is close to zero again. The temperature values taken by the air sampler in Hohenpeißenberg around 7 am or 7 pm are ranging from 0 °C to –10 °C for the 6th to the 12th of January 2024 (see Fig. 4.4). Since the heat labile fraction of INP is interpreted as biological fraction, the low amount of biological INP in samples from the 6th to the 9th of January can be related to low biological activity due to low temperatures. In the samples from the 10th to the 12th of January a fraction in heat labile INP is clearly differenciable from the heated sample. Especially on the 11th and the 12th of January a large amount of total INP is activated above –10 °C. As the temperatures during these days were still below 0 °C, the biological INP are likely coming from long range transport.

All filter samples from the 27th of February to the 28th of February in Hohenpeißenberg, shown in Fig. 4.22, are showing high activation temperatures of INP and a large biological fraction. Only on the 29th of February the biological fraction is smaller for INP of concentrations from 10^{-3} INP/l on (see Fig. 4.23). On the first of March, a considerable biological fraction exists for all measured INP in INDA.

Due to technical problems during the sampling process in Eriswil and Hohenpeißenberg, filter samples from the 10th of January from 7 am on and filters from the 26th of February in Hohenpeißenberg are missing (see table 7.2).

5.2.3 INP Contrasts between Hohenpeißenberg and Eriswil

Separately for the two measurement periods, Figs. 5.1 and 5.2 are showing a comparison of filter samples from Eriswil under northeast wind conditions and corresponding filter samples from Hohenpeißenberg. The selection has been done based on the backward trajectories calculated for Eriswil (see Figs. 4.14 and 4.15). As Hohenpeißenberg is situated northeast from Eriswil, this assignment is representing corresponding air masses. For the temporal assignment a time difference of 24 hours between Hohenpeißenberg and Eriswil was chosen. A 24-hour-difference matched the transport time best in most cases. Choosing individual time differences for each filter pair did not lead to crucial changes in the results. In individual cases, the trajectories indicated a longer or shorter transport time between the two measurement sites. Since the fixed time difference for every filter pair enhances the comparability, this approach has been applied. In individual cases the forward trajectories of Hohenpeißenberg also did not match the corresponding backwards trajectories of Eriswil. As the trajectories are calculated based on data with an accuracy of 0.25 °, the calculations of air mass movements have a spatial uncertainty of at least 25 km. The uncertainty is enhanced due to possible deviations in the configurations of the HYSPLIT model used for the calculations of the trajectories of Hohenpeißenberg and Eriswil. Due to technical problems during the sampling process some filter samples are missing. Comparison plots including those filters are missing.

The filter assignment shows very similar INP curves for Hohenpeißenberg and Eriswil for Plots a and b in Fig. 5.1. There is no relevant contrast between the activated INP in Eriswil and Hohenpeißenberg. During the presented days in Plot a and b there is a neglectibly small heat labile fraction in both INP samples from Eriswil and Hohenpeißenberg. During both presented days in these plots the Bise cloud exists over Eriswil. The VISSS images taken in Eriswil, discussed earlier, are showing falling ice crystals for both the 8th and the 10th of January in Eriswil (see Figs. 4.9 and 4.11).

In plots c and d of Fig. 5.1 there is a clearly visible contrast between total activated INP between Hohenpeißenberg and Eriswil. The INP in both Hohenpeißenberg samples of these days are activated at about 5 K higher than the INP from Eriswil samples of both days. This contrast applies for the whole INP concentration range presented in plots c and d of Fig. 5.1. The contrast is enhanced by a large fraction of heat labile INP for the Hohenpeißenberg samples. The corresponding samples from Eriswil do not show a large fraction in heat labile INP. It is also notable that the contrast in activated INP goes up to very low temperatures of nearly –30 °C, indicating an activation and loss of these INP via precipitation during transport. As there is no high-reaching cloud that time in Eriswil, the INP have to be lost through precipitation during transport of the air masses between Hohenpeißenberg and Eriswil.

This indicates a loss of INP between Hohenpeißenberg and Eriswil for plots c and d, while plots a and b do not show such a loss. A Bise cloud was present over Eriswil during the days of all four plots in Fig. 5.1. The missing heat labile fraction in Eriswill indicates the lost INP in plot c and d to be biological. This could explain the INP data of plot a and b being very similar for Eriswil and Hohenpeißenberg, since there is only a very small or no heat labile fraction in both INP curves. The loss of mainly biological INP can be explained by the temperatures in the Bise cloud only reaching around –9 °C (see Fig. 4.1). Since this temperature is too high to explain the loss of INP activated higher than around –15 °C, the real temperature in the cloud might have been lower than suggested by the temperature model.

Fig. 5.2 is showing comparison plots of Hohenpeißenberg and Eriswil INP data for the second measurement period. The second measurement period is differing from the first one by higher temperatures (see Figs. 4.1 and 4.2). All four plots of the second measurement period are very similar. The INP data of Hohenpeißenberg as well as the one from Eriswil is showing a large fraction in heat labile INP. The activated total INP as well as the activated INP of the heated samples from Hohenpeißenberg and Eriswil are overlapping. This is showing a contrast to plots c and d of Fig. 5.1. This indicates that all INP in the air masses of Hohenpeißenberg stay in the air and get transported to Eriswil.

The temperature model is suggesting temperatures of around –2 °C during this Bise cloud at Eriswil. Even considering an inaccuracy of ± 5 °C in the model, the temperatures of –7 °C are too high for activating INP, since the sampled INP only start to be activated at this temperature. Ice crystals in the cloud did not form and thus no INP were removed from the air masses during their transport from Hohenpeißenberg to Eriswil. This gets proven by VISSS data that was taken during the third Bise cloud event, which does not show any falling crystals (see Figs. 7.11 and 7.12).

5.2.4 Comparison of the two Measurement Periods

Both comparison plots from Eriswil and Hohenpeißenberg in Figs. 4.24 and 4.25 are showing an overview about all filter sample analysis that were presented in the result chapter. The plots are showing the total activated INP separately for the two measurement periods. The first period is presented in purple and the second one in orange colours.

Both plots are indicating generally higher concentrations (more INP frozen at higher temperatures) in the second measurement period compared to the first measurement period (Figs. 4.24 and 4.25). This can be explained by the presence of higher temperatures in Hohenpeißenberg as well as in Eriswil in the end of February compared to the beginning of January. The higher temperatures lead to a higher biological activity in the environment, which generally enhances the production of biological INP.

5.2.5 Impact of Seeding Activity

Figs. 4.26 and 4.27 show the comparison of INP data for filters sampled in Eriswil while seeding activities with silver iodide were performed 15 minutes upstream of the measurement site (red) compared to sampled filters without any seeding impact. Both plots show an overlap of data without any visible contrast in activation range of INP. This shows that the seeding activities in Eriswil did not affect the collected INP samples. The artificial INP that were emitted by an UAV at cloud level were either immediately activated or the time between injection of the silver iodide and the INP sampling at Eriswil was too short for allowing the down-mixing of the seeding INP toward the surface where the sampling took place.

6 Conclusions

The goal of this thesis was the determination of a spatial contrast in ice nucleation activity between the two research sites Hohenpeißenberg and Eriswil during a Bise wind situation. In the first hypothesis, it was suggested that the ice nucleating particles in the air masses are removed during transport from Hohenpeißenberg to Eriswil in the presence of suitable cloud conditions that allow for heterogeneous ice formation to take place.
Air samples were taken and analyzed for activation of INP at both sites. Since the temperatures differed between the two measurement periods (06.01.–12.01.2024 and 26.02.–01.03.2024), the results were interpreted separately.

The results show a spatial contrast for the concentration of activated INP only in two out of eight direct INP comparison plots. These two samples were characterized by a high concentration of biological INP in Hohenpeißenberg and a low concentration of biological INP in Eriswil. The measurements showed that the concentration of biological INP is dependent on environmental temperatures as well as on the origin of the air masses. The temperatures during the sampling time for the samples with spatial difference in biological INP fraction were the lowest compared to all other direct comparisons. The VISSS detected falling ice crystals in Eriswil during the sampling time on which the two plots are based on. The amount of ice crystals in addition seems to be enhanced by the presence of a second higher level cloud above the Bise cloud. The sedimentation of ice crystals toward the ground is connected to a loss of INP from the air. Presumably, this removal process was occurring during the entire pathway of the air mass between Hohenpeißenberg and Eriswil.

The four direct INP comparison plots from the second measurement period showed very similar INP activation at both sites. This period was characterized by higher temperatures and a high biological INP concentration in Hohenpeißenberg and Eriswil. The similar INP activation characteristics show that the INP are not removed during transport of the air mass between the two sites. The VISSS was showing no sedimenting ice crystals during the overlapping sampling times from this second, warm period.

The separate INP analysis from the cold and warm Bise situations show that low temperatures are necessary for the existence of a spatial contrast in INP activation between Hohenpeißenberg and Eriswil. This shows that the loss of INP between the two sites is not necessarily or not only coupled to the sole existence of a Bise cloud above Eriswil. A Bise cloud above Eriswil was formed also at the end of February, when there was no spatial contrast in INP activation between the two sites. The persistence of the Bise cloud above Eriswil can therefore not be explained sufficiently by a contrast in INP.

Based on the analysis of the samples from the cold and warm Bise periods, the first hypothesis of this thesis can be evaluated. A general statement that INP are removed during transport of air masses from Hohenpeißenberg to Eriswil cannot be confirmed. A more refined perspective seems to be required. According to this study, INP are only removed on their way from Hohenpeißenberg to Eriswil when (a) a Bise cloud is present and (b) temperatures in this Bise cloud layer are low enough to allow for heterogeneous freezing, a subsequent growth of ice crystals and, finally, a sedimentation of these ice crystals and the incorporated INP via precipitation. Generally, the hypothesis is supported by the measurements for days of subzero temperatures at ground level in Eriswil and a high biological fraction in the air over Hohenpeißenberg.

The second hypothesis stated, that the performed seeding experiments upstream of Eriswil would not affect the INP concentration at this site. Comparison plots for INP activation in air samples taken during the seeding experiments and the control days showed no significant difference in INP activation. The measurements are therefore supporting the hypothesis. The lack in silver iodide particles in the filter samples taken in Eriswil shows that (a) all silver iodide particles were activated and thus removed through precipitation directly after seeding or (b) the time difference of 15 minutes between seeding and sampling was too short for the turbulence in the PBL to transport the silver iodide particles to the sampled ground-level air masses.

While conclusions on the two hypotheses of this study could be appropriately drawn, further and refined studies should be aspired in order to enable a generalization of the presented and discussed findings. The number of samples taken at both sites needs to be increased to increase the statistical significance of the results. The characterization of the environmental conditions at both sites should be refined. Since the temperature was identified as important parameter, temperature data should be based on in situ measurements instead of model data. This could be realized by radiosondes. The characterization of the air mass pathway could also be improved by in situ measurements since the HYSPLIT model is prone to uncertainties. In situ measurements could be realized by the use of an aircraft to probe the air masses between Hohenpeißenberg and Eriswil. Only by doing so, actual case studies of the removal of INP between the two sites under cold Bise conditions will be realizable.

Literature

Agresti, A., & Coull, B. A. (1998). Approximate is better than “exact” for interval estimation of binomial proportions. *The American Statistician*, *52*(2), 119–126. https://doi.org/10.1080/00031305.1998.10480550

Andrews, D. G. (2000). *An introduction to atmospheric physics*. Cambridge.

Bailey, M. P., & Hallett, J. (2009). A comprehensive habit diagram for atmospheric ice crystals: Confirmation from the laboratory, AIRS II, and other field studies. *Journal of the Atmospheric Sciences*, *66*(9), 2888–2899. https://doi.org/10.1175/2009JAS2883.1

Cantrell, W., & Heymsfield, A. (2005). Production of ice in tropospheric clouds: A review. *Bulletin of the American Meteorological Society*, *86*(6), 795–808. https://doi.org/10.1175/BAMS-86-6-795

Deutscher Wetterdienst (German Meteorological Service), C. D. C. (2024). Stündliche Stationsmessungen der Lufttemperatur in 2 m Höhe in °C: OBS_DEU_PT1H_T2M: 2024-01-01 / 2024-03-02. https://cdc.dwd.de/portal/

Fletcher, N. H. (2009). *The chemical physics of ice*. Cambridge University Press.

Foth, A. (2017). *Optimal estimation of water vapour profiles using a combination of raman lidar and microwave radiometer* [Dissertation]. Universität Leipzig.

Gong, X., Radenz, M., Wex, H., Seifert P., Ataei, F., Henning, S., Baars, H., Barja, B., Ansmann, A., & Stratmann, F. (2022). Significant continental source of ice-nucleating particles at the tip of Chile’s southernmost Patagonia region. *Atmospheric Chemistry and Physics*, (22), 10505–10525. https://doi.org/10.5194/acp-22-10505-2022

Götz, G., Mészáros, E., & Vali, G. (1991). *Atmospheric particles and nuclei*. Akadémiai Kiadó és Nyomda Vállalat.

Granwehr, T. (2022). In Eriswil beobachten Forschende den Hochnebel: Projekt der ETH Zürich: Auf dem Rapierplatz werden wissenschaftliche Wolkenmessungen durchgeführt, um so die Niederschlagsbildung zu untersuchen. Weshalb sich der Ort von Eriswil besonders gut dafür eignet. *BZ Berner Zeitung*, 9. https://ethz.ch/content/dam/ethz/special-interest/usys/iac/iac-dam/documents/group/wolke/lohmann/Cloudlab-ETH-Medienberichte-20220228.pdf

Hartmann, M., & Simon, D. (2024). Inp measurements with INDA & LINA: Version 2.0.1.

Hartmann, S., Niedermeier, D., Voigtländer, J., Clauss, T., Shaw, R. A., Wex, H., Kiselev, A., & Stratmann, F. (2011). Homogeneous and heterogeneous ice nucleation at LACIS: Operating principle and theoretical studies. *Atmospheric Chemistry and Physics*, *11*(4), 1753–1767. https://doi.org/10.5194/acp-11-1753-2011

Henneberger, J., Ramelli, F., Spirig, R., Omanovic, N., Miller, A. J., Fuchs, C., Zhang, H., Bühl, J., Hervo, M., Kanji, Z. A., Ohneiser, K., Radenz, M., Rösch, M., Seifert, P., & Lohmann, U. (2023). Seeding of supercooled low stratus clouds with a UAV to study microphysical ice processes: An introduction to the CLOUDLAB project. *Bulletin of the American Meteorological Society*, *104*(11), E1962–E1979. https://doi.org/10.1175/BAMS-D-22-0178.1

Holden, M. A., Campbell, J. M., Meldrum, F. C., Murray, B. J., & Christenson, H. K. (2021). Active sites for ice nucleation differ depending on nucleation mode. *Proceedings of the National Academy of Sciences of the United States of America*, *118*(18), e2022859118. https://doi.org/10.1073/pnas.2022859118

Hoose, C., & Möhler, O. (2012). Heterogeneous ice nucleation on atmospheric aerosols: A review of results from laboratory experiments. *Atmospheric Chemistry and Physics*, *12*(20), 9817–9854. https://doi.org/10.5194/acp-12-9817-2012

Karlsson, K. G. (1997). *An introduction to remote-sensing in meteorology*. SMHI.

Korolev, A. (2007). Limitations of the Wegener–Bergeron–Findeisen mechanism in the evolution of mixed-phase clouds. *Journal of the Atmospheric Sciences*, *64*(9), 3372–3375. https://doi.org/10.1175/JAS4035.1

Libbrecht, K. G. (2008). Crystal growth in the presence of surface melting and impurities: An explanation of snow crystal growth morphologies. http://arxiv.org/pdf/0810.0689v1

Maahn, M., Moisseev, D., Steinke, I., Maherndl, N., & Shupe, M. D. (2024). Introducing the video in situ snowfall sensor (VISSS). *Atmospheric Measurement Techniques*, *17*(2), 899–919. https://doi.org/10.5194/amt-17-899-2024

Meyers, R. A. (Ed.). (2002). *Encyclopedia of physical science and technology* (3. ed.). Academic Press.

Mossop, S. C. (1980). The mechanism of ice splinter production during riming. *Geophysical Research Letters*, *7*(2), 167–169. https://doi.org/10.1029/GL007i002p00167

Proske, U., Bessenbacher, V., Dedekind, Z., Lohmann, U., & Neubauer, D. (2021). How frequent is natural cloud seeding from ice cloud layers (< -35 °C) over Switzerland? *Atmospheric Chemistry and Physics*, *21*(6), 5195–5216. https://doi.org/10.5194/acp-21-5195-2021

Roe, G. H. (2005). Orographic precipitation. *Annual Review of Earth and Planetary Sciences*, *33*(1), 645–671. https://doi.org/10.1146/annurev.earth.33.092203.122541

Schönwiese, C.-D. (2013). *Klimatologie* (vierte). UTB.

Seifert, P. (2011). *Dust-related ice formation in the troposphere: A statistical analysis based on 11 years of lidar observations of aerosols and clouds over Leipzig*. https://ul.qucosa.de/id/qucosa:11232

Stein, A. F., Draxler, R. R., Rolph, G. D., Stunder, B. J. B., Cohen, M. D., & Ngan, F. (2015). NOAA's HYSPLIT atmospheric transport and dispersion modeling system. https://doi.org/10.1175/BAMS-D-14-00110.1

Sze, K., Wex, H., Hartmann, M., Skov, H., Massling, A., Villanueva, D., & Stratmann, F. (2023). Ice-nucleating particles in northern Greenland: Annual cycles, biological contribution and parameterizations. *Atmospheric Chemistry and Physics*, (23), 4741–4761. https://doi.org/10.5194/acp-23-4741-2023

Vali, G., DeMott, P. J., Möhler, O., & Whale, T. F. (2015). Technical note: A proposal for ice nucleation terminology. *Atmospheric Chemistry and Physics*, *15*(18), 10263–10270. https://doi.org/10.5194/acp-15-10263-2015

Vali, G. (1971). Quantitative evaluation of experimental results an the heterogeneous freezing nucleation of supercooled liquids. *Journal of the Atmospheric Sciences*, *28*(3), 402–409. https://doi.org/10.1175/1520-0469(1971)028{\textless}0402:qeoera{\textgreater}2.0.co;2

Wanner, H., & Furger, M. (1990). The Bise-climatology of a regional wind north of the Alps. *Meteorology and Atmospheric Physics*, *43*(1-4), 105–115. https://doi.org/10.1007/BF01028113

Zhang, Y., Klein, S. A., Boyle, J., & Mace, G. G. (2010). Evaluation of tropical cloud and precipitation statistics of community atmosphere model version 3 using CloudSat and CALIPSO data. *Journal of Geophysical Research: Atmospheres*, *115*(D12). https://doi.org/10.1029/2009JD012006

7 Appendix

Table 7.1: Summary of ERI filter samples taken during both measurement periods in Eriswil.

ERI filter number	Type	Start (UTC)	End (UTC)	Note	Seeding
1	sample	2024-01-05 20:00	2024-01-06 08:00		
2	sample	2024-01-06 08:00	2024-01-06 20:00		
3	sample	2024-01-06 20:00	2024-01-07 08:00		
4	sample	2024-01-07 08:00	2024-01-07 20:00		
5	sample	2024-01-07 20:00	2024-01-08 08:00		
6	sample	2024-01-08 08:00	2024-01-08 20:00	15:12 & 15:52 UTC	
7	blank			LVS error	
8	blank			LVS error	
9	blank			LVS error	
10	blank			LVS error	
11	sample	2024-01-09 20:48	2024-01-10 08:35	manual start	

Continued on next page

Table 7.1: Summary of ERI filter samples taken during both measurement periods in Eriswil. (Continued)

ERI filter number	Type	Start (UTC)	End (UTC)	Note	Seeding
12	sample	2024-01-10 08:46	2024-01-10 20:00	manual start; washwater INDA: 6.750 ml	
13	blank				
14	sample	2024-01-10 20:03	2024-01-11 08:03	manual start	
15	sample	2024-01-11 08:03	2024-01-11 20:03		9:06, 13:05, 13:45, 14:22, 15:03 UTC
16	sample	2024-01-11 20:03	2024-01-12 07:57		
17	blank				
18	filter	2024-02-26 08:00	2024-02-26 20:00		
19	blank			LVS error	
20	filter	2024-02-26 20:19	2024-02-27 08:19	manual restart	
21	filter	2024-02-27 08:19	2024-02-27 20:19	after this sample, the data recording stopped	16:27,17:13 UTC
22	filter	2024-02-27 20:19	2024-02-28 08:19	no metadata	22:02,22:35 UTC
23	filter	2024-02-28 08:19	2024-02-28 20:19	no metadata	11:18,12:24 UTC
24	filter	2024-02-28 20:19	2024-02-29 08:19	no metadata	

Continued on next page

Table 7.1: Summary of ERI filter samples taken during both measurement periods in Eriswil. (Continued)

ERI filter number	Type	Start (UTC)	End (UTC)	Note	Seeding
25	filter	2024-02-29 08:19	2024-02-29 20:19	no metadata	
26	filter	2024-02-29 20:19	2024-03-01 08:19	no metadata	

Table 7.2: Summary of HPB filter samples taken during both measurement periods in Hohenpeißenberg.

Filter ID	Type	Start (UTC)	End (UTC)	Note
HPB_LV_001	sample	2024-01-05 07:18:55	2024-01-05 19:18:49	LINA error
HPB_LV_002	sample	2024-01-05 19:18:57	2024-01-06 07:18:46	
HPB_LV_003	sample	2024-01-06 07:18:55	2024-01-06 19:18:46	INDA washvolume 6.75 ml
HPB_LV_004	sample	2024-01-06 19:18:56	2024-01-07 07:18:48	INDA washvolume 6.75 ml; manual image evaluation
HPB_LV_005	sample	2024-01-07 07:18:55	2024-01-07 19:18:46	
HPB_LV_006	sample	2024-01-07 19:18:52	2024-01-08 07:18:47	
HPB_LV_007	sample	2024-01-08 07:18:52	2024-01-08 19:18:48	
HPB_LV_008	sample	2024-01-08 19:18:55	2024-01-09 07:18:50	
HPB_LV_009	sample	2024-01-09 07:18:55	2024-01-09 19:18:47	

Continued on next page

Table 7.2: Summary of HPB filter samples taken during both measurement periods in Hohenpeißenberg. (Continued)

Filter ID	Type	Start (UTC)	End (UTC)	Note
HPB_LV_010	sample	2024-01-09 19:18:55	2024-01-10 07:18:47	INDA washvolume 6.75 ml
HPB_LV_011	sample	2024-01-10 07:18:56	2024-01-10 11:22:10	test emergency diesel generator; less volume filtered
HPB_LV_012	sample	2024-01-10 11:22:14	2024-01-10 14:19:25	until 13:17 test emergency diesel generator; less volume filtered
HPB_LV_013	blind	2024-01-10 14:20:54	2024-01-10 14:20:54	
HPB_LV_014	blind	2024-01-10 14:20:59	2024-01-10 14:20:59	
HPB_LV_015	sample	2024-01-10 19:00:13	2024-01-11 07:00:06	
HPB_LV_016	sample	2024-01-11 07:00:14	2024-01-11 19:00:06	INDA washvolume 6.75 ml
HPB_LV_017	sample	2024-01-11 19:00:12	2024-01-12 07:00:07	
HPB_LV_018	blind	2024-01-12 07:00:14	2024-01-12 07:00:28	
HPB_LV_019	blind	2024-01-12 07:00:32	2024-02-26 08:00:06	this filter was inside the Digitel sampling chamber between the two Bise periods
HPB_LV_020	sample	2024-02-26 08:00:11	2024-02-26 20:00:06	sucked out of filter holder (lost filter)

Continued on next page

Table 7.2: Summary of HPB filter samples taken during both measurement periods in Hohenpeißenberg. (Continued)

Filter ID	Type	Start (UTC)	End (UTC)	Note
HPB_LV_021	sample	2024-02-26 20:00:13	2024-02-27 08:00:03	
HPB_LV_022	sample	2024-02-27 08:00:09	2024-02-27 20:00:04	INDA washvolume 6.75 ml
HPB_LV_023	sample	2024-02-27 20:00:09	2024-02-28 08:00:04	
HPB_LV_024	sample	2024-02-28 08:00:12	2024-02-28 20:00:03	
HPB_LV_025	sample	2024-02-28 20:00:13	2024-02-29 08:00:03	
HPB_LV_026	sample	2024-02-29 08:00:13	2024-02-29 20:00:05	
HPB_LV_027	sample	2024-02-29 20:00:10	2024-03-01 08:00:04	

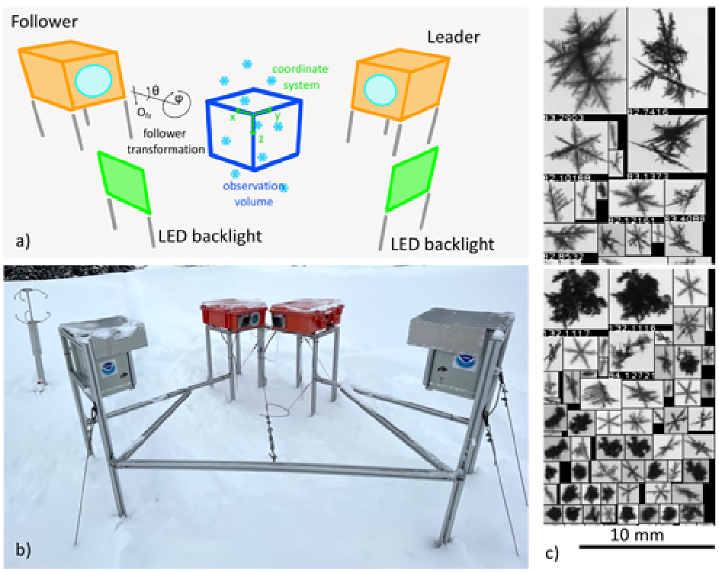

Figure 7.1: Setup of the VISSS (Maahn et al., 2024)

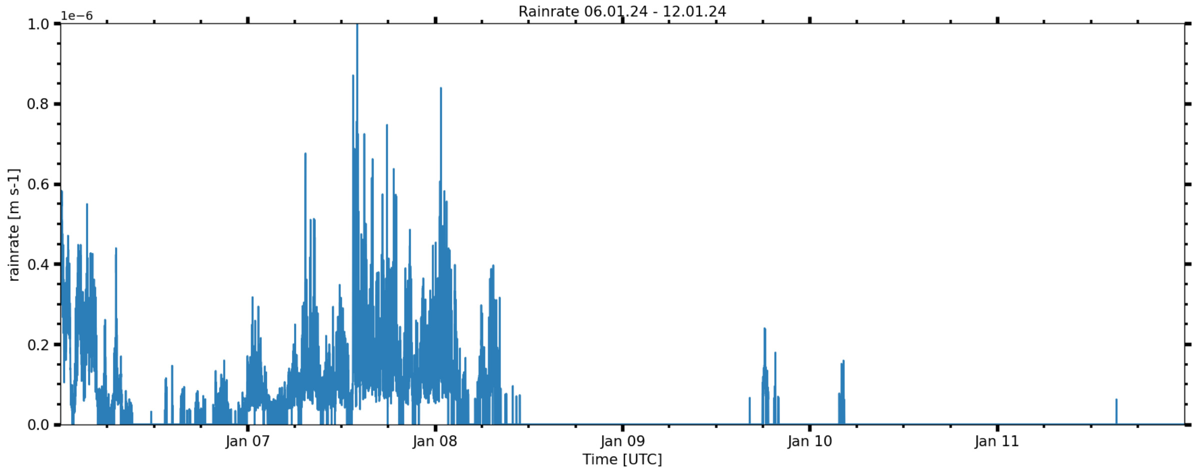

Figure 7.2: Rain rate (m/s) of the PARSIVEL in Eriswil for the first measurement period.

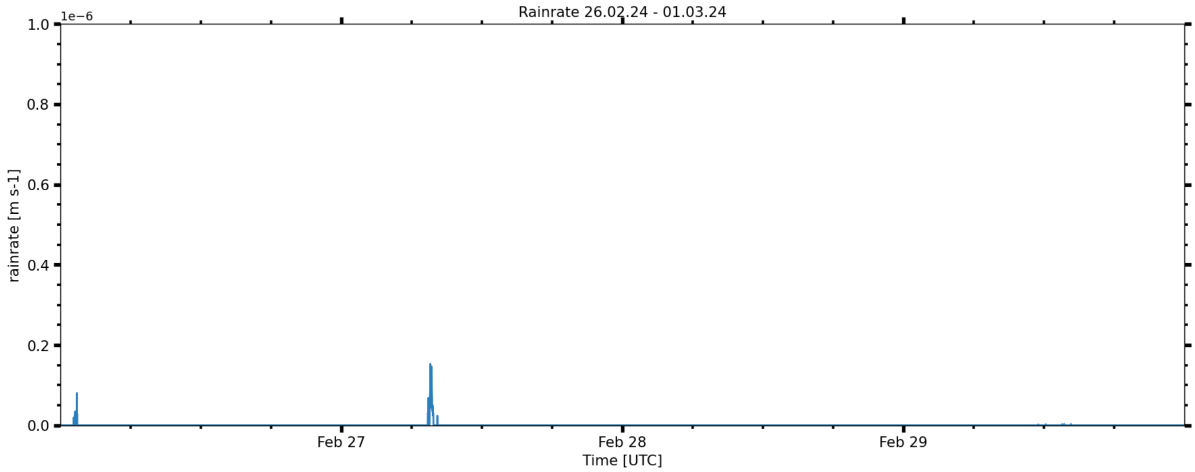

Figure 7.3: Rain rate (m/s) of the PARSIVEL in Eriswil for the second measurement period.

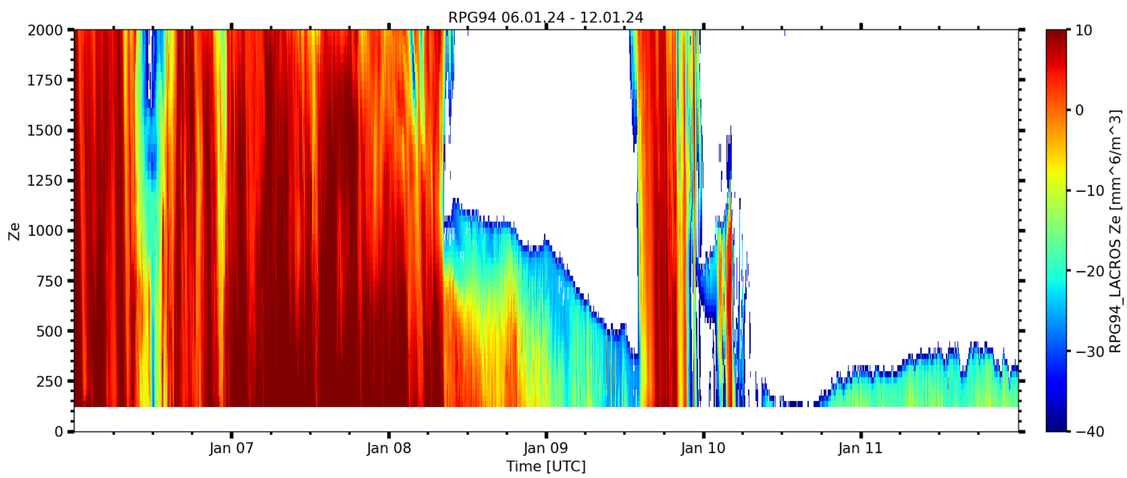

Figure 7.4: Radar reflectivity factor (dBZ) of the RPG 1MZ 0-2000

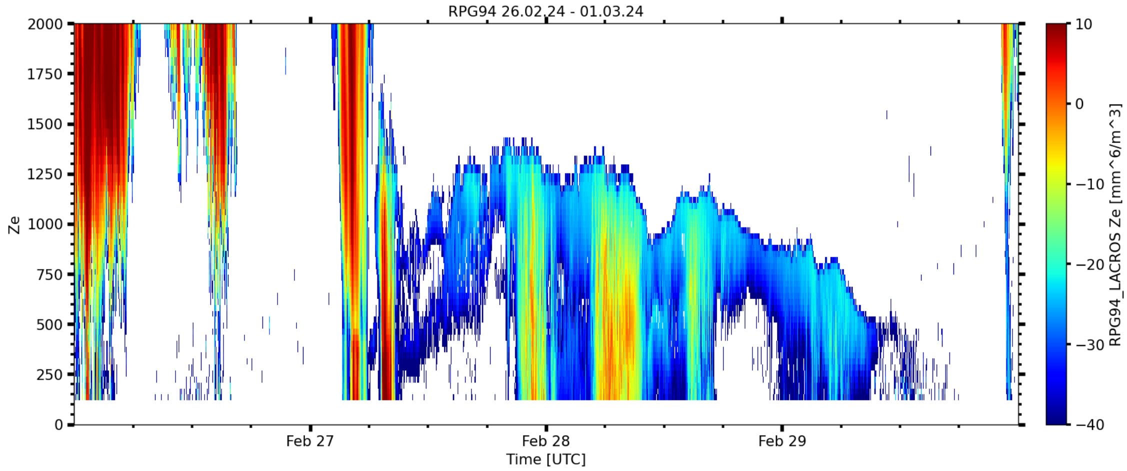

Figure 7.5: Radar reflectivity factor (dBZ) of the RPG 2MZ 0-2000

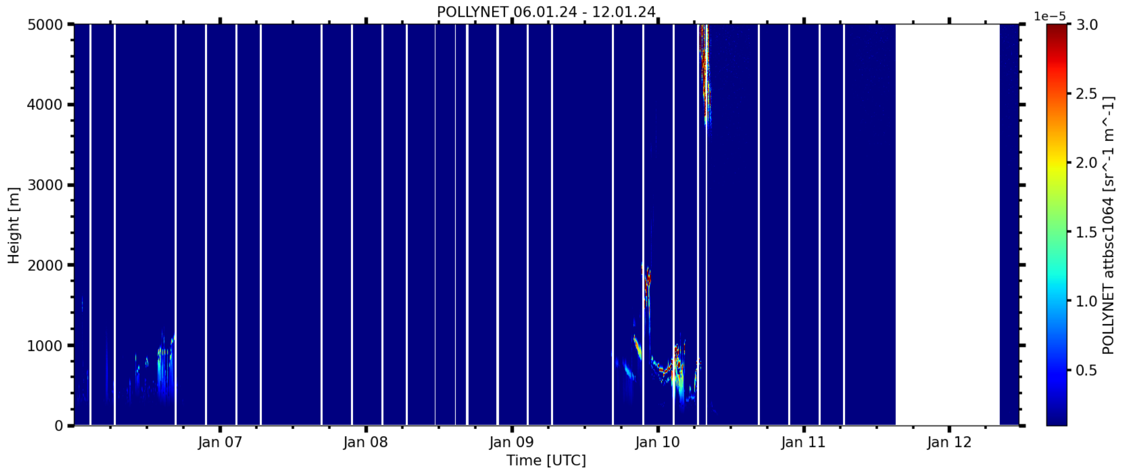

Figure 7.6: LIDAR result from the first measurement period in Eriswil.

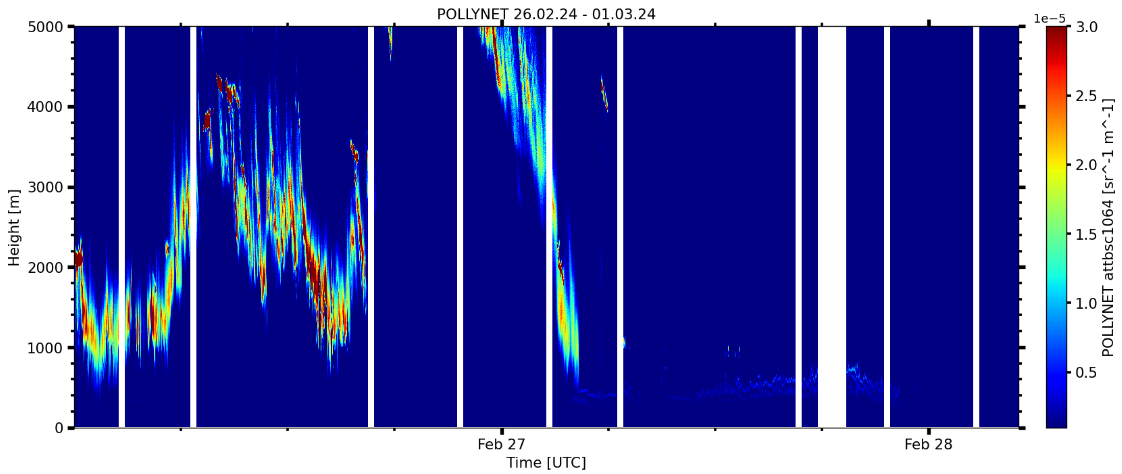

Figure 7.7: LIDAR result from the second measurement period in Eriswil.

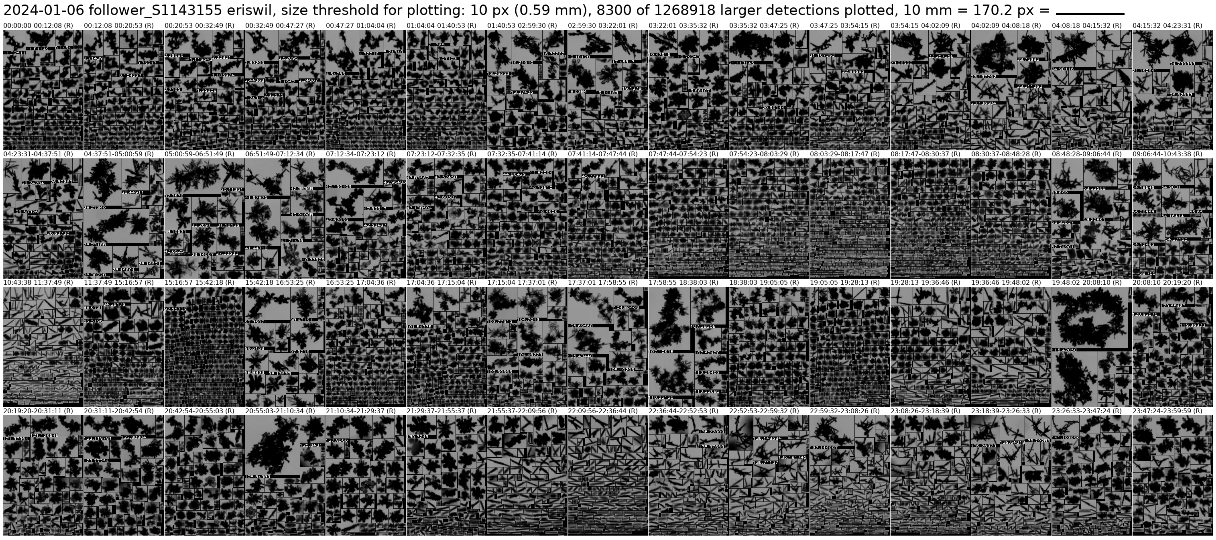

Figure 7.8: VISSS images from the 6th of January 2024 in Eriswil.

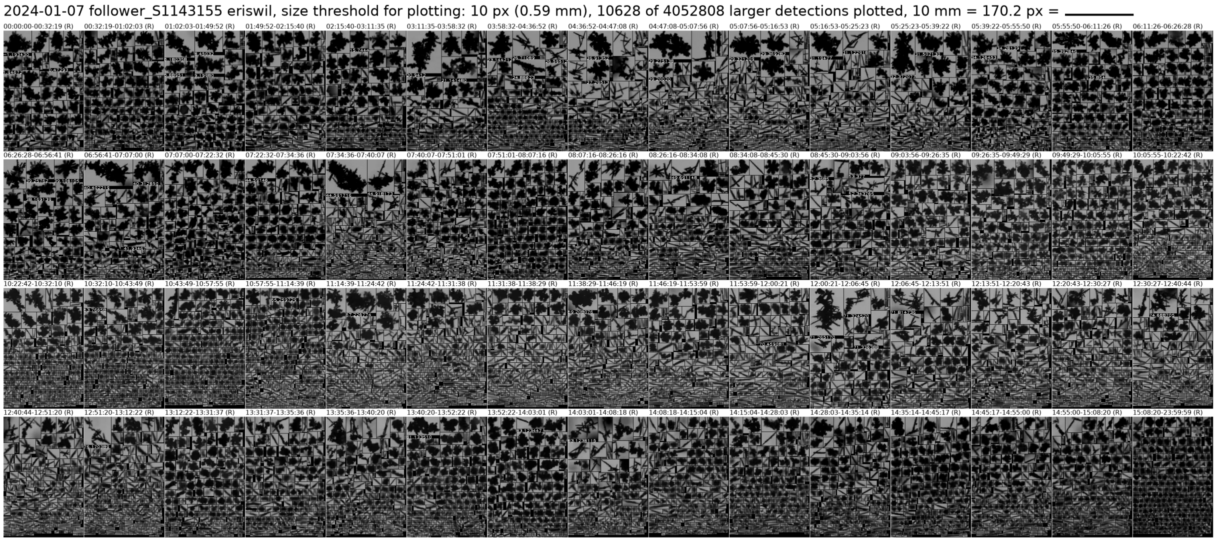

Figure 7.9: VISSS images from the 7th of January 2024 in Eriswil.

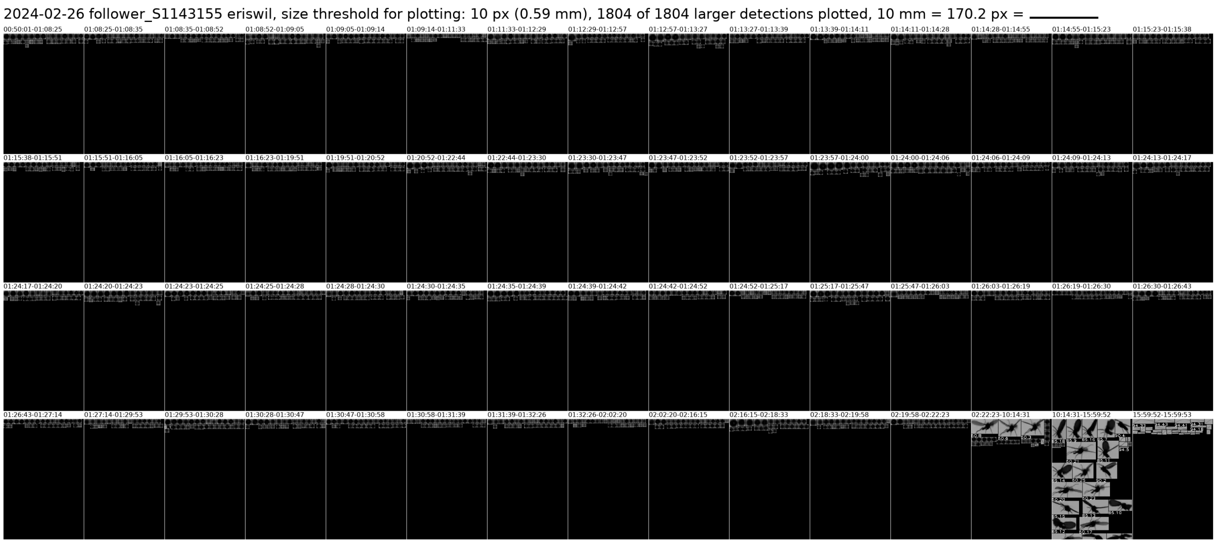

Figure 7.10: VISSS images from the 26th of February 2024 in Eriswil.

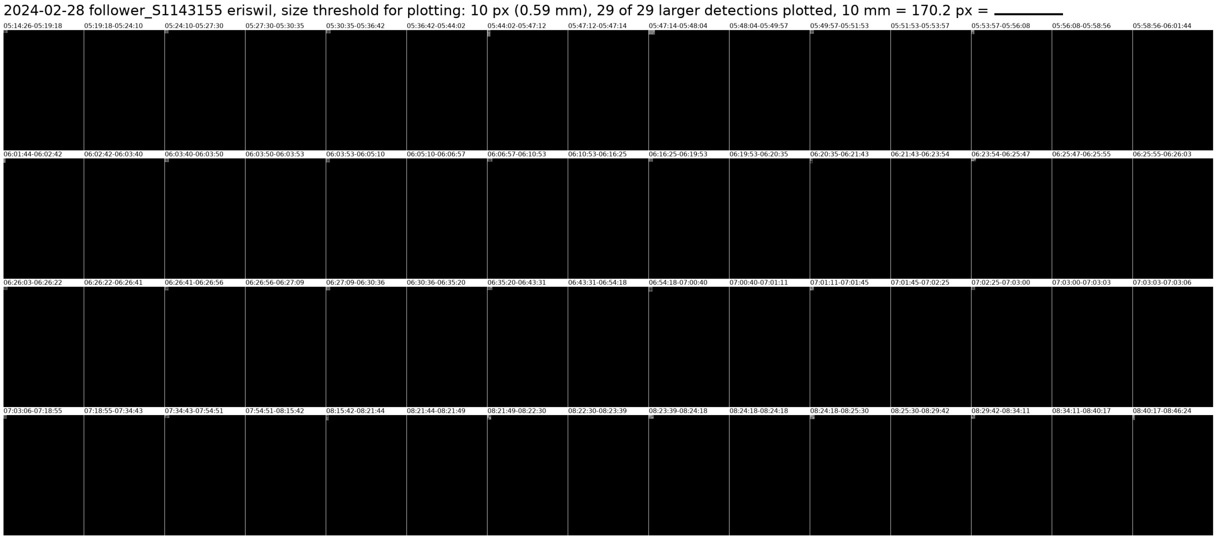

Figure 7.11: VISSS images from the 28th of February 2024 in Eriswil.

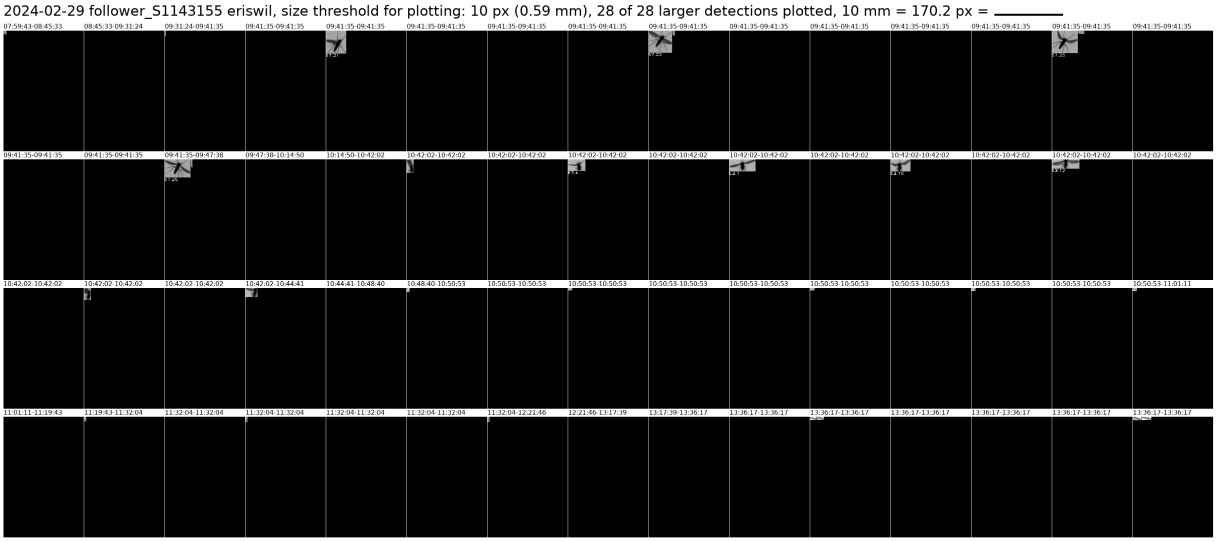

Figure 7.12: VISSS images from the 29th of February 2024 in Eriswil.

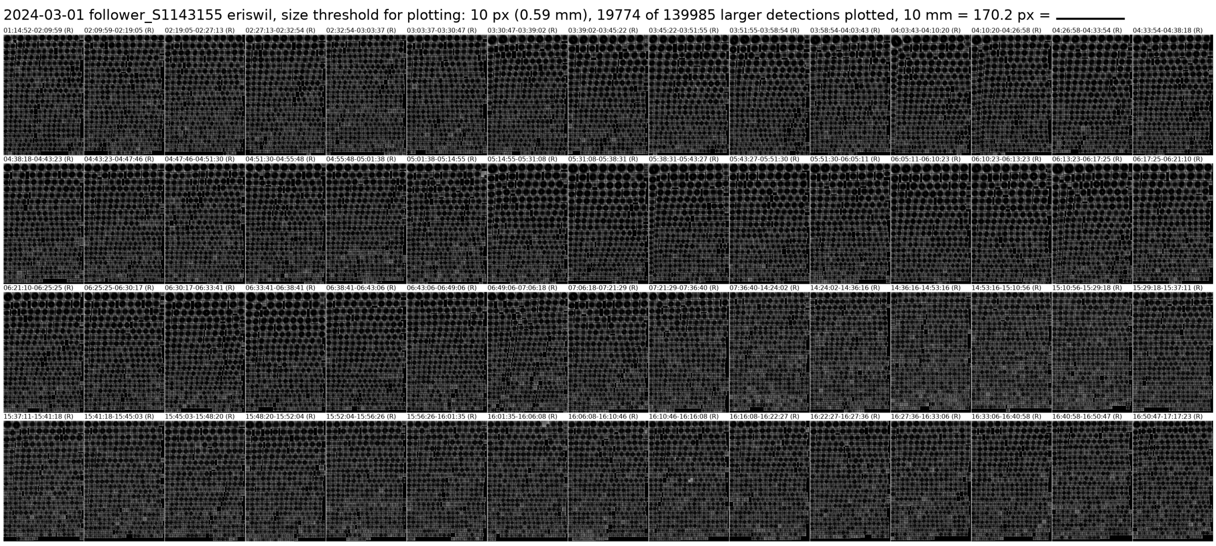

Figure 7.13: VISSS images from the 1st of March 2024 in Eriswil.

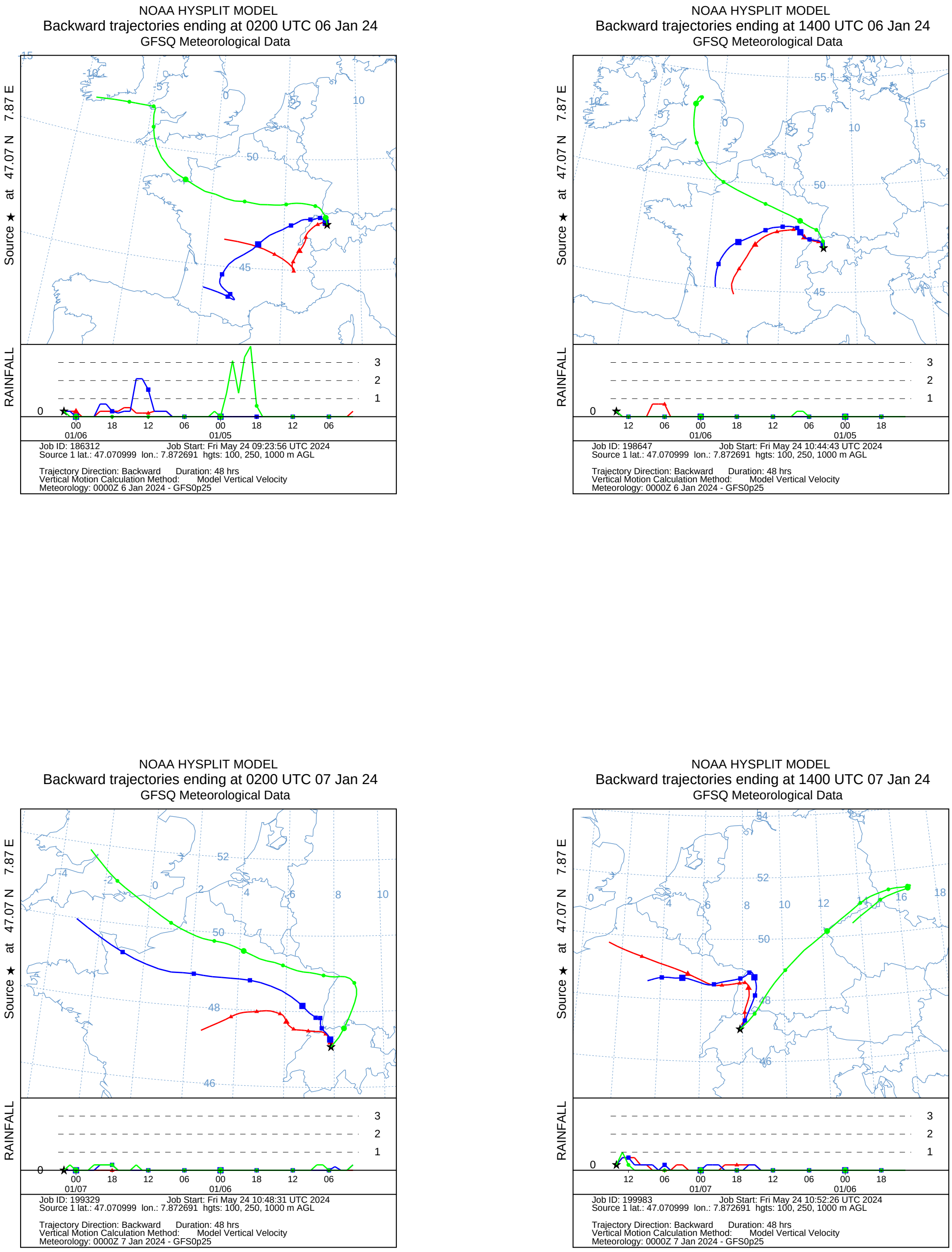

Figure 7.14: Backward trajectories for Eriswil for the 6th and 7th of January 2024. (Model: Stein 2015)

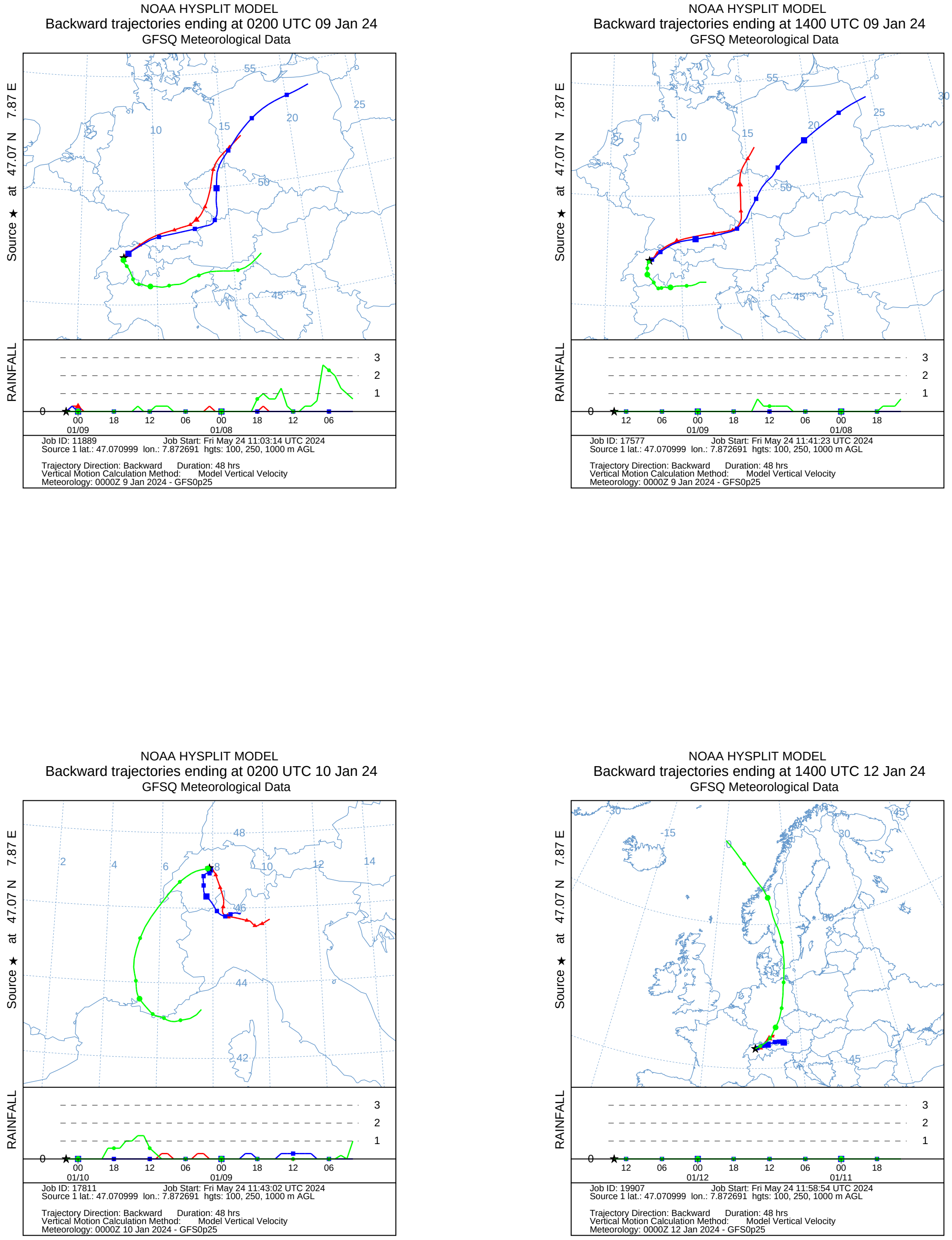

Figure 7.15: Backward trajectories for Eriswil for the 9th and 10th of January 2024. (Model: Stein 2015)

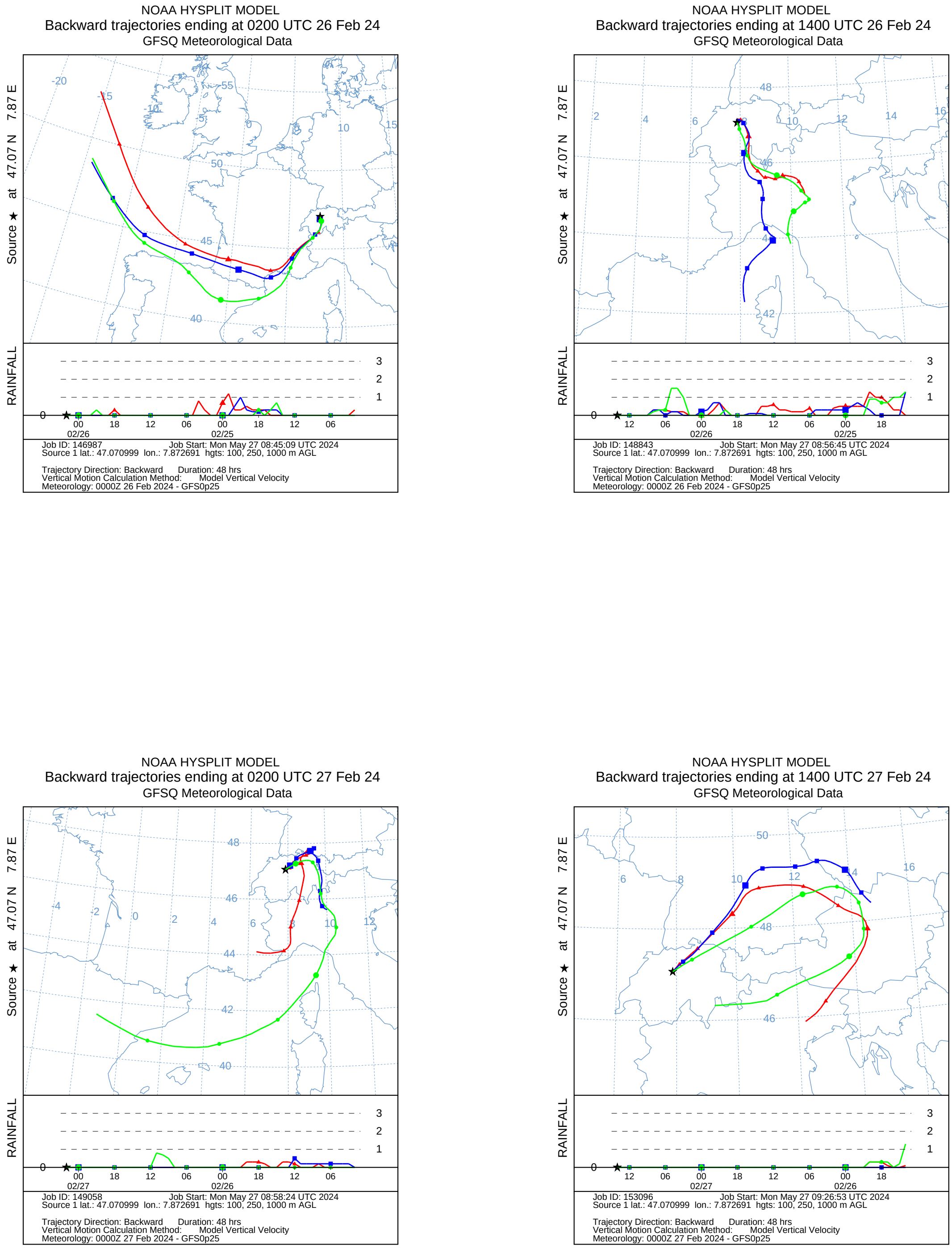

Figure 7.16: Backward trajectories for Eriswil for the 26th and 27th of February 2024. (Model: Stein 2015)

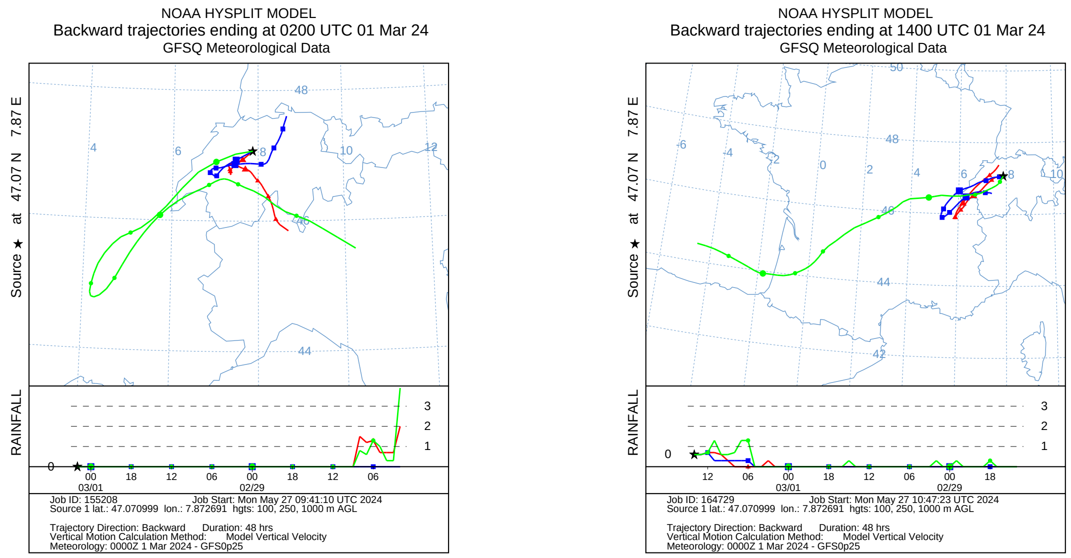

Figure 7.17: Backward trajectories for Eriswil for the 1st of March 2024. (Model: Stein 2015)

Figure 7.18: Photo of filter samples from Eriswil during the sample preparation. (Photo: Anna Miller)

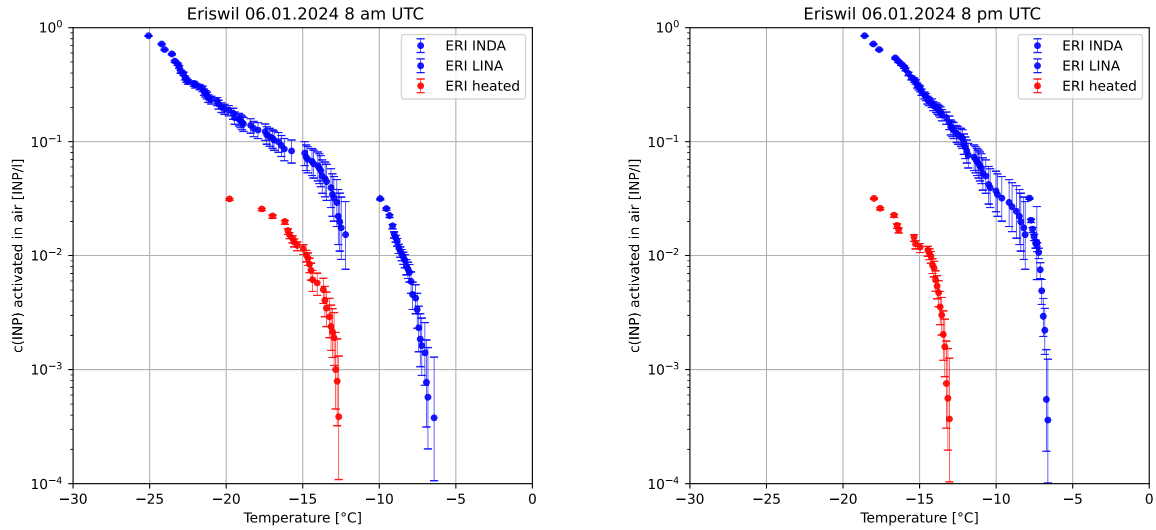

Figure 7.19: INP results for filters 1 and 2 taken on the 6th of January 2024 in Eriswil.

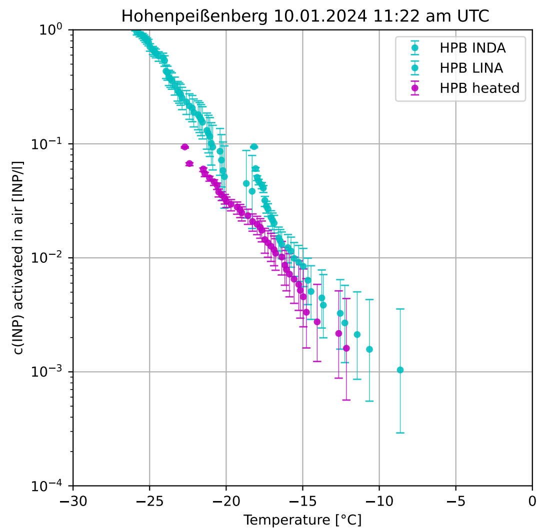

Figure 7.20: Freezing analysis result for the sample of the 10th of January 2024 at 11:22 am from Hohenpeißenberg. Limited comparability of the sample due to a decisively shorter sample time of circa 4 hours.

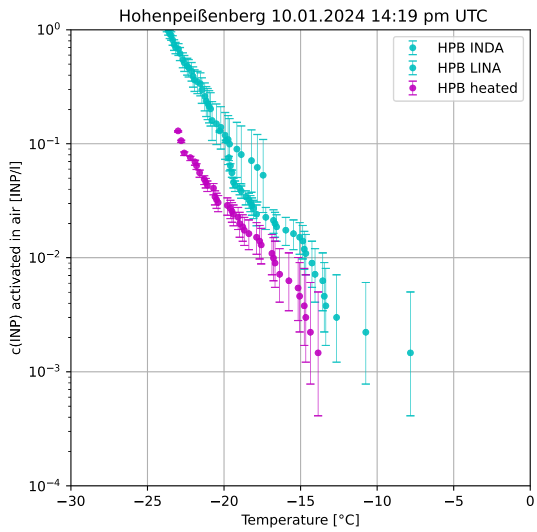

Figure 7.21: Freezing analysis result for the sample of the 10th of January 2024 at 14:19 pm from Hohenpeißenberg. Limited comparability of the sample due to a decisively shorter sample time of circa 3 hours.